

Global detector network to search for high-frequency gravitational waves (GravNet): conceptual design

Dorian Amaral¹, Diego Blas^{1,12}, Yuliia Borysenkova^{1,14}, Dmitry Budker^{2,3,4,5}, Alessandro D'Elia⁶, Giorgio Dho⁶, Alejandro Díaz-Morcillo¹¹, Daniele Di Gioacchino⁶, Sebastian Ellis¹⁷, Claudio Gatti⁶, Benito Gimeno⁹, Jordan Gué¹, Stefan Horodenski⁸, Saarik Kalia¹, Younggeun Kim^{2,3}, Tom Krokotsch⁷, Tomas Kvietkauskas^{1,14}, Adrián Lambies-Asensio⁹, Carlo Ligi⁶, Giovanni Maccarrone⁶, Giovanni Mazzitelli⁶, Juan Monzó-Cabrera¹¹, José R. Navarro-Madrid¹¹, José Reina-Valero¹⁰, Alessio Rettaroli⁶, Kristof Schmieden⁸, Tim Schneemann¹³, Matthias Schott⁸, Simone Tocci⁶, Sandro Tomassini⁶, Oleg Tretiak^{2,3}, Luca Visinelli^{15,16}, Changhao Xu^{2,3}

¹ *Institut de Física d'Altes Energies (IFAE), The Barcelona Institute of Science and Technology, Campus UAB, 08193 Bellaterra (Barcelona), Spain*

² *PRISMA++ Cluster of Excellence, Institute of Physics, Johannes Gutenberg University, Mainz, Germany*

³ *Helmholtz Institute Mainz, 55099 Mainz, Germany*

⁴ *GSI Helmholtzzentrum für Schwerionenforschung GmbH, 64291 Darmstadt, Germany*

⁵ *Department of Physics, University of California, Berkeley, California 94720, USA*

⁶ *National Institute for Nuclear Physics, Italy*

⁷ *Universität Hamburg, Luruper Chaussee 149, 22761 Hamburg, Germany*

⁸ *Rheinische Friedrich-Wilhelms-Universität, Bonn, Germany*

⁹ *Instituto de Física Corpuscular (IFIC), CSIC-University of Valencia, Calle Catedrático Jose Beltrán Martínez, 2, 46980 Paterna (Valencia), Spain*

¹⁰ *Laboratorio Subterráneo de Canfranc, 22880 Canfranc-Estación (Huesca), Spain*

¹¹ *Departamento de Tecnologías de la Información y las Comunicaciones, Universidad Politécnica de Cartagena, Plaza del Hospital 1, 30202 Cartagena (Murcia), Spain.*

¹² *Institució Catalana de Recerca i Estudis Avançats (ICREA), Passeig Lluís Companys 23, 08010 Barcelona, Spain*

¹³ *Institute of Physics, Johannes Gutenberg University, Mainz, Germany*

¹⁴ *Grup de Física Teòrica, Departament de Física, Universitat Autònoma de Barcelona, 08193 Bellaterra (Barcelona), Spain*

¹⁵ *Dipartimento di Fisica "E.R. Caianiello", Università degli Studi di Salerno, Via Giovanni Paolo II, 132 - 84084 Fisciano (SA), Italy*

¹⁶ *Istituto Nazionale di Fisica Nucleare - Gruppo Collegato di Salerno - Sezione di Napoli, Via Giovanni Paolo II, 132 - 84084 Fisciano (SA), Italy*

¹⁷ *Theoretical Particle Physics and Cosmology (TPPC) Group, Department of Physics, King's College London, Strand, London, WC2R 2LS, UK,*

Abstract. We propose GRAVNET (Global detector network to search for high-frequency gravitational waves), a novel experimental scheme enabling the search for gravitational waves in the MHz to GHz frequency range. Such high-frequency gravitational waves could arise from a variety of phenomena connected to some of the most pressing and fundamental questions in modern cosmology. The GRAVNET concept is based on synchronous measurements of signals from multiple experimental measurement devices operating at geographically separated locations. While gravitational-wave-induced signatures may be present in the signal of a single detector, distinguishing them from instrumental or environmental noise is highly challenging. By analyzing correlations between signals from several distant detectors, the detection significance is substantially enhanced, while simultaneously enabling studies of the nature and origin of the gravitational-wave signal. In this work, we discuss the GRAVNET concept specifically in the context of cavities operated in strong magnetic fields, as these currently represent the most technically mature and experimentally advanced realization of the scheme. As part of this proposal, a first demonstration experiment using a non-superconducting cavity has been performed, providing the basis for the data-analysis strategies discussed in this work. Finally, we outline the prospects and future development of GRAVNET as a global network for high-frequency gravitational-wave searches.

Contents

1	Introduction	2
2	Theoretical Background	2
3	Experimental Setup	8
4	Network Operation	13
5	Analysis Considerations	16
6	Performance of GravNet	16
7	Conclusion and Outlook	22

1 Introduction

The detection of gravitational waves (GWs) stands out as one of the most groundbreaking achievements in 21st-century physics. These subtle signals have revolutionized our understanding of Nature despite having been observed only in the band from 10 Hz to 10 kHz scanned by ground-based interferometers [1], and suggested as the origin of a nHz signal present in pulsar-timing arrays [2]. In both cases, the original proposals searching for these signals were once considered futuristic, but today’s results are a testament to the foresight of their pioneers.

This remarkable accomplishment ushers in new and immediate challenges. One of the most pressing issues is expanding the sensitivity to gravitational waves across other spectral regions. The discovery potential here is extraordinary: from profound inquiries into the primordial universe, like stochastic GWs from inflation or phase transitions, to unique insights into new astrophysical phenomena, such as black holes of a variety of masses, of primordial or astrophysical origin [3, 4]. Several proposals have emerged to address this challenge for frequencies below 10 kHz. For instance, GWs from the lowest detectable frequencies of 10^{-18} Hz (with wavelengths on the order of the size of the visible Universe today) may impact the properties of the cosmic microwave background [5], while space-based laser interferometers will probe the mHz band [3]. The next generation of ground-based observatories [6] and pulsar-timing efforts [7], together with other techniques ranging from large atom interferometers to astrometry, provide broad coverage of GWs from 10^{-18} Hz to 10 kHz [8].

The Global Network of Detectors to Search for Gravitational Waves (GRAVNET) aims to establish a cohesive initiative targeting similar coverage of high-frequency gravitational waves (HFGWs) in the MHz to GHz range. A key difference in the search for HFGWs, as compared to searches at lower frequencies, is the difficulty in producing substantial GWs above 10 kHz in standard astrophysical scenarios [4, 9, 10]. The reason is that gravitation, being an extremely weak interaction, requires large coherent sources (such as accelerated stars or black holes) for the efficient production of GWs. However, the forces required to induce motions that generate GWs well above 10 kHz would destroy standard astrophysical objects ¹. By contrast, HFGWs may be generated copiously by processes related to some of the most pressing open questions about our Universe: violent phenomena in the early Universe (such as primordial phase transitions, inflation, or topological defects), thermal fluctuations of the primordial plasma and dark matter [4, 9]. This shows that the absence of abundant astrophysical sources enables the search of signals from fundamental physics, motivating a vigorous exploration of the HFGW band. Furthermore, this uncharted territory may harbor surprises yet to be unveiled. We set $\hbar = c = \epsilon_0 = 1$ unless otherwise stated.

2 Theoretical Background

2.1 Sources of transient or coherent (and persistent) HFGWs

A well-motivated class of sources of high-frequency gravitational waves (HFGWs) are primordial black holes (PBHs), which may be produced in the early Universe and could constitute a significant fraction, or even all, of the dark matter [12–14]. In addition to PBHs formed directly from large primordial density fluctuations, compact objects may also arise from the gravitational collapse of particle dark matter overdensities, such as those associated with weakly interacting massive particles near the Griest–Kamionkowski bound [15, 16]. For WIMP masses of order $\mathcal{O}(100 \text{ TeV})$, the resulting compact objects can have masses as low as $\sim 10^{-10} M_\odot$, placing them naturally in the mass range relevant for HFGW emission. Regardless of their origin, only sufficiently compact dark sector objects can act as efficient HFGW sources as the GW frequency emitted scales with the compactness \mathcal{C} as $f_g = \mathcal{C}^{3/2}/(3\sqrt{3}\pi GM_{\text{tot}})$ [17], leaving diffuse dark MACHOs irrelevant.

A fraction of PBHs is expected to reside in binary systems that emit gravitational waves. For a quasi-circular binary of two equal-mass PBHs with individual masses M_{bh} , combined merger mass M_{PBH} , and orbital radius

¹ The smallest objects made of nuclear matter have a diameter in the order of 10 km. If rotating with 1 kHz, the speed at the equator approaches the speed of light, which shows that such objects cannot emit HFGWs. It is worth mentioning that the collisions of neutron stars may produce GWs at MHz frequencies, whose discovery would clarify new aspects of matter at high densities [11].

r_b , the gravitational-wave frequency is bounded from above by the value at the innermost stable circular orbit² (ISCO),

$$\omega_g \equiv 2\pi f_g \approx 14 \text{ GHz} \left(\frac{10^{-6} M_\odot}{M_{\text{PBH}}} \right) \left(\frac{r_{\text{ISCO}}}{r_b} \right)^{3/2}, \quad (1)$$

where M_\odot is the solar mass and $r_{\text{ISCO}} \simeq 36 \text{ km} (M_{\text{bh}}/M_\odot)$ denotes the ISCO radius [10]. Here, $r_{\text{ISCO}}/r_b \leq 1$, and Eq. (1) therefore defines the ISCO frequency f_{ISCO} corresponding to $r_{\text{ISCO}}/r_b = 1$. We use f_{ISCO} as a reference value throughout this work.

As a result, HFGWs can be emitted by binaries of sufficiently light PBHs one achieves GHz or larger frequencies. The emission of gravitational waves causes the binary orbit to shrink [10], leading to a characteristic chirp, i.e. an increase in the GW frequency with time. This provides a natural scan over resonant detector frequencies. While the GW frequency lies within the resonance band of an oscillator, its response is resonantly enhanced, significantly increasing the signal. However, requiring the source to remain in the resonance band for more than $Q_t \sim 10^5$ cycles implies $M_{\text{bh}} \lesssim 10^{-12} M_\odot$ at $\omega_g \simeq 5 \text{ GHz}$ [18],

$$N_{\text{cyc}} \approx 10^{-3} \left(\frac{10^{-6} M_\odot}{M_{\text{bh}}} \right)^{5/3} \left(\frac{10^5}{Q_t} \right) \left(\frac{1 \text{ GHz}}{\omega_g} \right)^{5/3}. \quad (2)$$

This estimate is conservative: the effective bandwidth is larger for cavities that are not fully rung up, and heavier PBHs generate significantly stronger signals even if they do not remain resonant for the full ring-up time. We therefore defer a detailed treatment of higher PBH masses and the merger regime to future work.

Interestingly, this mass range overlaps with a notoriously difficult-to-constrain region of PBH parameter space, in which PBHs can still constitute a significant fraction of the dark matter [12]. The expected event rate and signal strength were studied in Ref. [19]. Assuming PBHs account for all of dark matter with a narrow mass function peaked at $M_{\text{bh}} \sim 10^{-12} M_\odot$, one expects order one event per year producing a sufficiently long-lived GW signal with strain amplitude³ $h_0 \sim 10^{-31}$ at Earth with $\omega_g \simeq 5 \text{ GHz}$. At MHz frequencies, corresponding to $M_{\text{bh}} \sim 10^{-6} M_\odot$, the expected strain can be as large as $h_0 \sim 10^{-24}$ [19]. Recent work indicates that inspiral signals and eccentric orbits can further enhance the prospects, potentially generating additional harmonics in the HFGW band [20, 21].

HFGWs may also arise from ultralight bosonic dark matter [22]. If bosons of mass m_φ exist, spinning black holes of mass $M_{\text{bh}} \simeq M_\odot (10^{-11} \text{ eV}/m_\varphi)$ can develop a macroscopic boson cloud through superradiance [23, 24]. The cloud emits nearly monochromatic gravitational waves through different processes [25]. The most relevant for our work are those generated by boson annihilation processes, $\varphi + \varphi \rightarrow h$, at a frequency corresponding to twice the mass of the boson,

$$\omega_g \equiv 2\pi f_g = 2m_\varphi \approx 3 \times 10^4 \text{ Hz} \left(\frac{m_\varphi}{10^{-11} \text{ eV}} \right), \quad (3)$$

while other emission channels are possible, in particular if self-interactions of the bosonic field are included [25–27]. For $m_\varphi \gg 10^{-11} \text{ eV}$, the emitted GWs lie in the HFGW regime; however, efficient superradiance at these masses requires sub-solar-mass black holes, implying a primordial origin and a nontrivial dark sector.

If such superradiant systems exist in the Milky Way, one expects strains of order $h_0 \sim 10^{-25}$ (10^{-28}) at MHz (GHz) frequencies [28]. In contrast to PBH binaries, the GW frequency in this case is fixed by the boson mass, necessitating active frequency scanning in resonant searches. The duration of the emission phase is typically of order days to months for the gravitational coupling $\alpha \equiv GM_{\text{bh}} m_\varphi \sim 0.1$ at GHz frequencies, decreasing for higher frequencies. For these reasons, and because early PBH inspirals naturally provide broadband and slowly evolving signals, we focus primarily on PBH sources in the context of this discussion of GRAVNET.

Finally, HFGWs can also originate from processes in the primordial Universe. Inflation, first-order phase transitions, thermal fluctuations, topological defects, and related phenomena generically produce stochastic gravitational-wave backgrounds with spectra that can extend into the MHz–GHz range [4, 29–31]. A particularly robust example is the so-called cosmic gravitational-wave microwave background, which is an unavoidable prediction of the Standard Model supplemented by inflation [9, 29]. These signals form a persistent and isotropic background arriving from the earliest moments of the Universe. Several models predict characteristic strains of order $h_0 \sim 10^{-29}$ (10^{-34}) at MHz (GHz) frequencies [9].

2.2 Detection Methods for High-Frequency Gravitational Waves

Detecting gravitational waves (GWs) at frequencies above $\mathcal{O}(10 \text{ kHz})$ is challenging with established GW technologies, both because of the detector response and because of readout/noise limitations. For laser interferometers, the

² At smaller orbital separations, the system enters a relativistic inspiral and merger phase, during which HFGWs are still emitted, although the simple Newtonian description breaks down.

³ For simplicity, we model the GW as a monochromatic plane wave $h^{\mu\nu} \approx h_0^{\mu\nu} e^{i(\omega_g t - \vec{k} \cdot \vec{x})}$, with $\mu, \nu = 0, 1, 2, 3$ and $h_0^{\mu\nu} \sim \mathcal{O}(h_0)$.

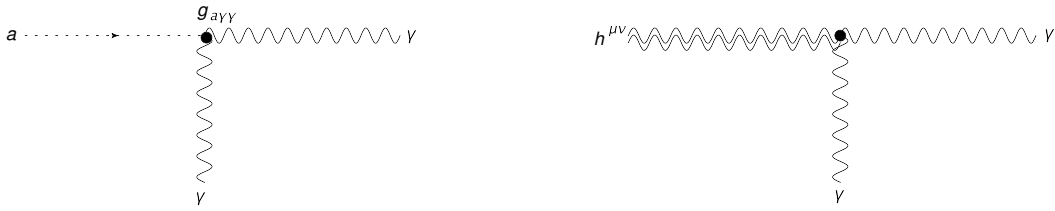


Fig. 1. Comparison of axion–photon conversion in a magnetic field (left) and gravitational-wave–to–photon conversion in a strong electromagnetic background (right), i.e. the quadratic interaction of EM fields γ with GWs $h^{\mu\nu}$, illustrating the close analogy between the two processes exploited in cavity-based searches.

response of long Fabry–Pérot arm cavities becomes strongly frequency dependent at $f_g \equiv \omega_g/(2\pi) \gtrsim \mathcal{O}(10 \text{ kHz})$, as the GW period becomes comparable to (or shorter than) the photon storage time and light travel time in km-scale arms [10]. Recent analyses have emphasized that, in the shot-noise limited regime, interferometers can nonetheless exhibit narrow high-frequency sensitivity features at multiples of optical free spectral ranges, and that detector configurations can in some cases be tuned to scan such narrow bands [32–34].⁴ At the same time, extending interferometric searches deep into the $\gtrsim 10 \text{ kHz}$ regime requires dedicated characterization of the readout chain and instrumental backgrounds at these frequencies, which is currently not standard in the large-scale GW-detector program.

A second traditional approach is based on mechanical resonators (“Weber bars” and their modern descendants) [10]. These devices are typically optimized for operation near their mechanical resonance frequencies (historically in the kHz band), and their sensitivity generally degrades at much higher frequencies. Nonetheless, resonant acoustic and phonon-trapping concepts have been proposed to target higher-frequency bands [35].

Overall, HFGW detection remains comparatively less explored than the sub-kHz regime. Motivated by the potentially transformative implications of any detection in the MHz-GHz band, a growing body of work has recently surveyed and advanced a range of HFGW concepts [4, 9]. This is also reflected by new proposals and re-analyses using existing precision experiments, including re-interpretations of axion-haloscope data as HFGW searches [36]. Since gravitation is universal and cannot be shielded, the passage of a GW can in principle imprint itself on essentially any precise laboratory setup; this perspective underlies many of the emerging HFGW detection strategies.

In GRAVNET, we focus on one of the most promising directions for realistic progress in the near term across a broad frequency range: electromagnetic (EM) cavities operated in the presence of strong background EM fields, and in particular strong magnetic fields. This choice is motivated by (i) the existence of technically mature cavity and readout technology developed for axion and axion-like particle searches, and (ii) the ability to realize large and stable background fields $\mathcal{O}(10 \text{ T})$ in compact detector volumes, enabling competitive GW-to-EM transduction per detector size and resource footprint.

Two main cavity-based mechanisms have been considered in recent years. The first is the modification of cavity eigenmodes due to effective boundary deformations induced by the GW (sometimes phrased as “shape distortion” or parametric modulation) [28, 37]. The second is the generation of an effective EM current in the presence of a background EM configuration, commonly referred to as the inverse Gertsenshtein effect [18, 38]. The origin of the latter is straightforward: gravity couples universally to energy and momentum, and for EM fields the stress-energy tensor is quadratic in the field strength (or equivalently in A^μ at the level of interactions), implying an interaction of the schematic form shown in Figure 1. As a consequence, in the presence of a background EM field A_b^μ and a GW $h^{\mu\nu}$, a signal field A_s^μ can be generated. For a background oscillating at frequency ω_b , the induced signal appears at sideband frequencies $\omega_b \pm \omega_g$. In the following, we will mostly be concerned about the second mechanism, as it is the one where more progress can be achieved in the near future. Both are compared in [28], and the inverse Gertsenshtein effect is the leading effect for frequencies close to the resonant frequencies of the cavities, which also supports focusing on this effect for a range of frequencies of the GWs.

The inverse Gertsenshtein effect is reminiscent of phenomenology from axion–photon interactions which, for an axion field a with axion-photon coupling $g_{a\gamma}$, reads $\propto g_{a\gamma} a \vec{E} \cdot \vec{B}$, for which resonant radio-frequency cavities in strong magnetic fields constitute one of the leading experimental search strategies [39]. A key implication is that there exists substantial theoretical and experimental expertise—including mature cryogenic cavity operation, low-noise RF amplification, and precision spectral analysis—that can be repurposed for HFGW detection. Indeed, recent work has demonstrated the feasibility of re-analyzing haloscope data to place competitive constraints on monochromatic HFGWs in the GHz band [36].

⁴ For instance, Refs. [32, 33] discuss high-frequency response and sensitivity structures of operating interferometers and the possibility of accessing the kHz–tens-of-kHz range by adjusting optical parameters.

Two differences between cavity-based HFGW searches and cavity-based axion searches are worth emphasizing. First, many transient GW sources (e.g. compact-binary inspirals) naturally sweep through frequency, so the cavity does not necessarily need to be mechanically tunable, provided the signal remains within the resonant bandwidth long enough (e.g. $N_{\text{cyc}} \gtrsim Q_l$ in the simplified discussion of Sec. 2.1). In this case, the time evolution of $\omega_g(t)$ also sets the effective coherent integration time t_{int} , since the signal eventually leaves the resonant band.

Second, unlike conventional axion dark-matter signals (which are expected to be quasi-stationary and approximately isotropic in the Galactic frame), GW signals have a definite propagation direction and polarization content, and they induce correlated responses across spatially separated detectors with predictable time delays. This enables additional discriminants and analysis handles that are central to GRAVNET: coincidence tests, baseline-dependent correlation searches, and (for persistent signals) daily modulation and directional inference using Earth rotation.

2.3 Interaction of High Frequency Gravitational Waves with Electromagnetic Cavities

In the following, we work explicitly in the framework of the inverse Gertsenshtein effect, where the interaction of a gravitational wave with a static magnetic field is described in terms of an effective electromagnetic current. In this context, for a cavity within a static magnetic field, $\omega_b = 0$, the induced field A_s^t in Figure 1 oscillates at the frequency of the gravitational wave ω_g . This mode can be resonantly enhanced using (microwave) cavities. The sensitivity to its detection depends on various factors, including ω_g , the incoming direction of the GW, the strength of the external magnetic field $B_0 = |\vec{B}_0|$, as well as the coupling of the incoming GW to the different resonance modes of the cavity.

Assuming a GW signal described by a functional form of the strain $h(t)$, the inverse Gertsenshtein effect implies an induced effective current in an electromagnetic cavity in a static magnetic field, which is given by

$$j \simeq B_0 \omega_g h_0 e^{i\omega_g t}. \quad (4)$$

It is important to note that the above equation becomes more complicated for a realistic experiment, where the induced current depends on the orientation of the setup w.r.t. the incoming GW wave as well as its polarization, and the current j has to be convolved with the resonance curve and therefore the quality factor Q_l of the cavity. The width of the resonance curve is inversely proportional to the quality factor Q , and therefore large values of Q yield a large resonant enhancement of the signal. This is particularly true if the signal lasts for enough cycles to fully ‘load’ the cavity ($N_{\text{cyc}} \gtrsim Q_l$) and reach a stationary regime. This has been used to build sensitivity estimates for searches of, for instance, PBHs [40], since the signal frequency during the inspiral phase of the merger varies as

$$\dot{f} = 4.62 \times 10^2 \left(\frac{M_{\text{PBH}}}{10^{-9} M_\odot} \right)^{5/3} \left(\frac{f_g}{\text{GHz}} \right)^{11/3} \frac{\text{GHz}}{\text{s}}, \quad (5)$$

which yields values of 10^{-6} GHz/s to 10^9 GHz/s for PBH merger masses between $M_{\text{PBH}} = 10^{-15} M_\odot$ and $M_{\text{PBH}} = 10^{-7} M_\odot$ for frequencies in the range of interest, $2 \text{ GHz} \leq f_g \leq 8 \text{ GHz}$. For comparison, the bandwidth of an electromagnetic cavity at a center frequency of 5 GHz with quality factors of 25×10^3 and 5×10^5 , corresponds to 2×10^{-4} GHz and 10^{-5} GHz. This leads to signal times within the cavity bandwidth between 10 s, which is long enough to integrate the signal with existing analysis approaches, to as low as 10^{-14} s, as can be seen in Tab. 1.

In order to estimate the experimental sensitivity, the deposited energy from HFGWs must be determined, which is given by the integrated deposited power. By approximating the resonance curve as a rectangular step function, where the width is given by the bandwidth $b = (f_0/Q_l)$, and assuming $P_{\text{sig}}(\omega_g) = P_{\text{sig}}(\omega_0)$ and \dot{f} to be constant within the narrow bandwidth of the cavity, the deposited energy is calculated as [40]

$$E = P_{\text{sig}} \frac{f_0}{Q_l} \frac{1}{\dot{f}}. \quad (6)$$

The EM power induced by the GW is calculated in the stationary limit where the cavity is fully rung up as [36]

$$P_{\text{sig}} = \frac{\beta}{1 + \beta} \frac{\omega_g}{2\mu_0} h_{\times,+}^2 \langle B_0^2 \rangle Q_l C_{\text{GW}}^{\times,+} V, \quad (7)$$

where β is the antenna coupling coefficient, V the volume of the cavity, B_0 the magnetic field strength, and h the GW strain. The factor $C_{\text{GW}}^{\times,+} = (\eta_{\text{GW}}^{\times,+})^2$ describes the coupling of the GW to the cavity mode as defined in [36], where η_{GW} is instead used in the conventions of [18, 20]. This coupling depends on the angle between the incoming GW and the B -field, ranging from 0 to 10^{-2} , where the maximum value and the average over all incident angles

$M_{\text{PBH}}[M_{\odot}]$	f_{ISCO} [GHz]	f_0 [GHz]	\dot{f} [Hz/s]	Δt [s], $Q_l = 5 \times 10^4$	Δt [s], $Q_l = 1 \times 10^5$	Δt [s], $Q_l = 5 \times 10^5$
10^{-15}	2×10^9	2	5.87×10^2	6.82×10^1	3.41×10^1	6.82
10^{-15}	2×10^9	5	1.69×10^4	5.92	2.96	5.92×10^{-1}
10^{-15}	2×10^9	8	9.46×10^4	1.69	8.46×10^{-1}	1.69×10^{-1}
10^{-13}	2×10^7	2	1.26×10^6	3.16×10^{-2}	1.58×10^{-2}	3.16×10^{-3}
10^{-13}	2×10^7	5	3.64×10^7	2.75×10^{-3}	1.37×10^{-3}	2.75×10^{-4}
10^{-13}	2×10^7	8	2.04×10^8	7.85×10^{-4}	3.92×10^{-4}	7.85×10^{-5}
10^{-11}	2×10^5	2	2.72×10^9	1.47×10^{-5}	7.34×10^{-6}	1.47×10^{-6}
10^{-11}	2×10^5	5	7.84×10^{10}	1.28×10^{-6}	6.38×10^{-7}	1.28×10^{-7}
10^{-11}	2×10^5	8	4.39×10^{11}	3.64×10^{-7}	1.82×10^{-7}	3.64×10^{-8}
10^{-9}	2×10^3	2	5.87×10^{12}	6.82×10^{-9}	3.41×10^{-9}	6.82×10^{-10}
10^{-9}	2×10^3	5	1.69×10^{14}	5.92×10^{-10}	2.96×10^{-10}	5.92×10^{-11}
10^{-9}	2×10^3	8	9.46×10^{14}	1.69×10^{-10}	8.46×10^{-11}	1.69×10^{-11}
10^{-7}	2×10^1	2	1.26×10^{16}	3.16×10^{-12}	1.58×10^{-12}	3.16×10^{-13}
10^{-7}	2×10^1	5	3.64×10^{17}	2.75×10^{-13}	1.37×10^{-13}	2.75×10^{-14}
10^{-7}	2×10^1	8	2.04×10^{18}	7.85×10^{-14}	3.92×10^{-14}	7.85×10^{-15}

Table 1. Time GWs from a PBH merger stay within the bandwidth of a cavity Δt depending on the cavities resonance frequency f_0 , PBH merger mass M_{PBH} and loaded quality factor of the cavity Q_l .

depend on the cavity mode and cavity geometry. This is illustrated for an idealized cylindrical cavity assuming the TM_{010} mode in Figure 2 and typical values are given in Tab. 3.

A detailed calculation of the signal power is derived in the proper detector frame in [18] and in the transverse-traceless (TT) frame in [36]. This calculation requires the choice of a reference frame (or ‘gauge’) and some debate has been devoted to this choice in recent literature. Ultimately, the result cannot depend on the choice of frame as long as all signal contributions are accounted for. In proper detector coordinates, the background magnetic field is perturbed as calculated in [18]; however, the cavity walls are also displaced by the GW, leading to an additional signal. In this work, we assume that the GW frequencies are large enough that the elastic forces in the cavity walls are negligible [20, 41], such that they behave as if they were freely falling. In this case, it is more convenient to use TT coordinates, in which the GW does not displace the cavity walls and the signal in Eq. (7) only emerges through the Gertsenshtein current, Eq. (4) [20, 36, 41, 42]

$M_{\text{PBH}}[M_{\odot}]$	f_g [GHz]	h_0	h_c	P_{sig} [W] ($h = h_0$)
10^{-15}	2.0	3.2×10^{-30}	2.7×10^{-22}	1.1×10^{-41}
10^{-15}	5.0	6.0×10^{-30}	2.3×10^{-22}	9.6×10^{-41}
10^{-15}	8.0	8.1×10^{-30}	2.1×10^{-22}	2.9×10^{-40}
10^{-11}	2.0	1.5×10^{-23}	5.7×10^{-19}	3.6×10^{-29}
10^{-11}	5.0	2.8×10^{-23}	4.9×10^{-19}	6.6×10^{-29}
10^{-11}	8.0	3.8×10^{-23}	4.6×10^{-19}	9.0×10^{-29}
10^{-7}	2.0	7.0×10^{-17}	1.2×10^{-15}	1.7×10^{-22}
10^{-7}	5.0	1.3×10^{-16}	1.1×10^{-15}	3.1×10^{-22}
10^{-7}	8.0	1.8×10^{-16}	9.8×10^{-16}	4.2×10^{-22}

Table 2. Electromagnetic power P_{sig} deposited in a cavity by a gravitational wave from a PBH merger of mass M_{PBH} . To calculate the strain h_0 using Eq. (8) at the resonance frequency $f_0 = f_g$, we consider a distance of one astronomical unit (AU) ($\sim 4.8 \times 10^{-9}$ kpc). To calculate the deposited power, we use Eq. (7) assuming the values discussed in Sec. 3 of $B_0 = 12$ T, $C_{\text{GW}} = 0.1$, $Q_l = Q_{\text{eff}} = \min(10^5, N_{\text{cyc}})$, and that the volume is independent of the frequency $V = 3 \times 10^{-4} \text{ m}^3$.

Radius [cm]	Cylinder height [cm]	Volume [m ³]	TM ₀₁₀ Freq [GHz]	Peak coupling C_{\max}^{\times}	Average coupling C_{GW}^{\times}
30	20	5.66×10^{-2}	0.38	0.27	0.16
10	20	6.28×10^{-3}	1.15	0.27	0.12
5	20	1.57×10^{-3}	2.29	0.27	0.08
2	20	2.50×10^{-4}	5.74	0.27	0.03
1	20	6.00×10^{-5}	11.47	0.27	0.02

Table 3. Resonance frequency of the TM₀₁₀ mode of a cylindrical cavity as a function of the cavity radius. Also shown are the assumed cavity heights and the average coupling factor to the cross polarization of a gravitational wave arriving from a random direction. Listed frequencies are given in GHz and rounded to two decimal places.

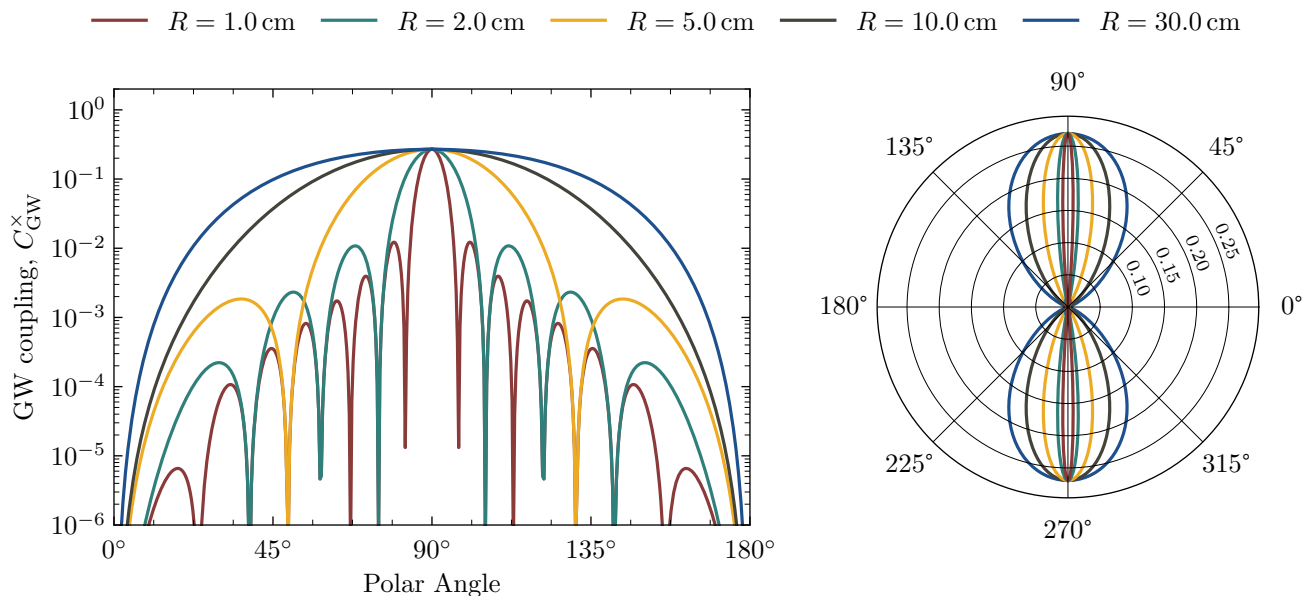


Fig. 2. The gravitational coupling C_{GW}^{\times} for an ideal TM₀₁₀ mode in a cylindrical cavity with fixed height $H = 20$ cm and various radii R . A uniform magnetic field is applied along the cavity symmetry axis. The coupling is maximized when the GW propagation direction is perpendicular to the magnetic field (at polar angles 90, 270°).

Table 2 gives an overview of the generated power in the envisioned cavities for various choices of the PBH mass under the assumptions described above. From Eq. (5), $\dot{f} \propto f_g^{11/3}$ which, from (6), leads to a dependence of the deposited energy on the frequency of the GW $E \propto f_g^{-8/3} b$, where b is the bandwidth of the resonator. For a PBH binary of equal masses M_{PBH} , the strain h_0 and characteristic strain h_c are calculated following [19] as

$$h_0 = 9.77 \times 10^{-34} \left(\frac{f_g}{\text{GHz}} \right)^{2/3} \left(\frac{M_{\text{PBH}}}{10^{-12} M_{\odot}} \right)^{5/3} \left(\frac{\text{kpc}}{D} \right), \quad (8)$$

and

$$h_c = 4.54 \times 10^{-28} \left(\frac{\text{GHz}}{f_g} \right)^{1/6} \left(\frac{M_{\text{PBH}}}{10^{-12} M_{\odot}} \right)^{5/6} \left(\frac{\text{kpc}}{D} \right), \quad (9)$$

where D is the distance in kpc. As shown in [20, 21, 43], for a signal with time-evolving frequency, the amount of power that ends up in the different modes requires an analysis in the time domain yielding larger values compared to those considering the stationary limit we applied above. Furthermore, the presence of eccentricity is also a source of higher tones, which also injects more energy in a situation with narrow resonances.

In the following chapter, we discuss several experimental considerations on the choice of the magnet systems, the cavity designs as well as the readout.

3 Experimental Setup

3.1 Magnet Systems

In the first version of GRAVNET, we foresee using two different types of magnet systems: one magnet system that can host a large-volume cavity with a base resonance frequency around 150 MHz, and a second magnet system aimed at a significantly smaller cavity volume with resonance frequencies in the GHz regime.

The large volume cavity will be placed in the FINUDA magnet [44, 45] at the Laboratori Nazionali di Frascati (LNF), which has an iron-shielded solenoid coil with a radius of 1.4 m and a length of 2.2 m; it is made from an aluminum-stabilized niobium superconductor (Figure 3). The magnet provides a homogeneous axial field of strength up to $B_0 = 1.1$ T. This large volume makes it possible to install a large cavity with a fundamental mode at a relatively low resonance frequency of 150 MHz. A newly constructed cryostat system will allow for the operation of the cavity at a temperature of 1.9 K. We refer to this as the FLASH cavity [46] in the following. The relatively low magnetic field strength is compensated for by its large volume. Moreover, for PBH-merger signals at these ‘low’ frequencies, the cavity ringing time reaches tens of milliseconds, exceeding the cavity lifetime and increasing the sensitivity as compared to mergers at higher frequencies.

The second type of magnets will be commercial systems integrated in cryostat systems. We foresee the initial version of GRAVNET having at least three such systems with a central magnetic field between 9 and 12 T, allowing the operation of a cavity at a base temperature of 10 mK (Figure 3). The field average over the usable cylindrical volume of $R = 5$ cm and $H = 30$ cm is about 20% lower than the central value.

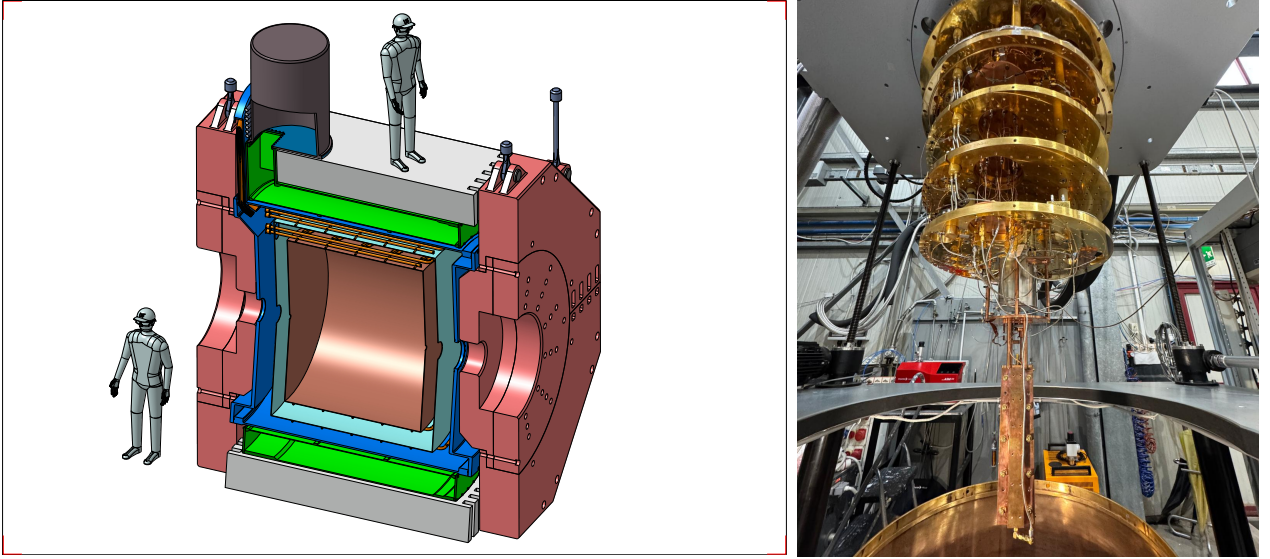


Fig. 3. Magnet and cryostat systems used in the GRAVNET program. Left: Schematic cross section of the FLASH magnet, indicating the magnet bore, cryostat structure, cooling connections and vacuum system (credits Cesidio Capoccia). Right: BlueFors dilution refrigerator with the installed 9 GHz cavity system at LNF, illustrating the compact cavity assembly and associated cabling inside the cryostat.

3.2 Cavity Design and Construction

The shape of the cavities defines their base resonance frequencies, their higher resonance modes, and also their coupling to HFGWs, labeled as $C_{\text{GW}}^{\times,+}$ in Eq. (7). Moreover, a trade-off between the volume of the cavities and the available volume of the magnetic field must be made. A significant advantage of cavities for GRAVNET compared to cavities in the context of axion-search experiments is that they do not need to be tunable to be sensitive to a significant parameter space of transient signals. This reduces the required R&D effort tremendously compared to dedicated axion-search experiments such as ADMX [47]. Given that the construction processes for large cavities

with volumes of several liters are significantly different from those for smaller cavities with a volume of several centiliters, these processes are discussed separately in the following sections.

For the baseline calculations of sensitivities within GRAVNET, we assume one cylindrical cavity placed in the FLASH magnet system optimizing the available volume. To achieve the lowest possible frequency with our largest magnet system, thus maximizing the signal a GW will induce, we foresee a cylindrical resonant cavity made of copper with a radius of 980 mm and a length of 1600 mm, corresponding to an inner volume of approximately 4.80 m^3 [46] (Figure 3). This optimizes the use of the available volume within the magnet and yields a resonance frequency of the TM_{010} mode of 129 MHz. The quality factor is expected to be about $Q \sim 5 \times 10^5$ [46]. The cavity will be hosted in a dedicated custom cryostat and cooled to 2 K by a cold compressor using LHe) from the LNF cryogenic plant. The cryostat and cryogenic components will be designed at LNF and purchased and installed within the GRAVNET project. We foresee that the cryostat will be composed of an external stainless-steel vacuum vessel, containing an aluminum-alloy radiation shield surrounding the cavity kept at about 70 K by cold gaseous helium (GHe). Both the cavity and the shield will be cooled in contact with pipes with flowing helium. The cryogenic plant [48] is already available at LNF.

The gravitational wave coupling to the TM_{010} mode was numerically evaluated for the given geometry of the FLASH cavity. In this mode, the electric field is dominated by the axial component E_z , which provides the main contribution to the GW cross-polarization coupling, C_{GW}^\times . Figure 4 presents C_{GW}^\times as a function of the GW incident angle measured with respect to the magnetic-field direction, \hat{z} . The coupling exhibits a clear angular dependence and reaches a maximum value of $C_{\text{max}}^\times = 0.24$ at a particular incident angle. This behavior indicates that the coupling efficiency is governed by the interplay between the TM_{010} field geometry and the GW polarization and incidence configuration. To incorporate the directional dependence under realistic observing

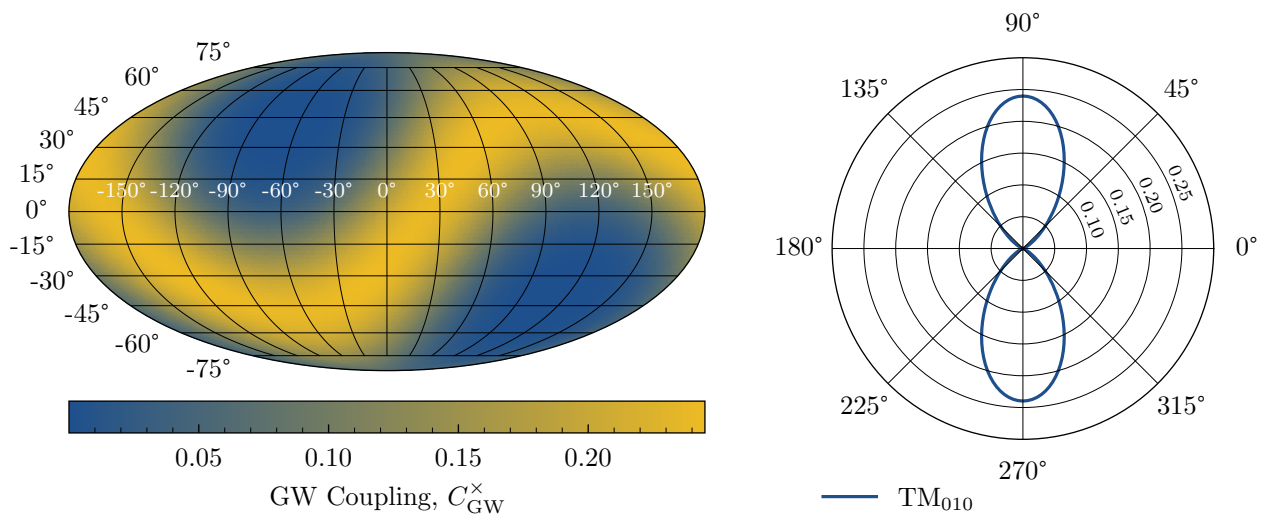


Fig. 4. Left: The GW coupling C_{GW}^\times for different sky positions of the GW source. The detector is located at LNF at 0:00 AM, and the magnetic field is aligned with the local zenith. **Right:** The GW coupling of a cross-polarized gravitational wave to the TM_{010} mode of the FLASH cavity.

conditions, we also evaluated the coupling for GWs arriving from various sky directions for the LNF site at 0:00 AM, as summarized in Figure 4. This calculation accounts for the location- and time-dependent transformation between the sky coordinates and the cavity (laboratory) frame. The resulting distribution demonstrates that the effective coupling of the FLASH cavity TM_{010} mode depends on the GW propagation direction, implying that the observation time and/or the instrument orientation can modulate the achievable coupling (and hence the signal sensitivity).

The situation is different for commercial magnet systems, as their cylindrical volume typically has a significantly larger height compared to their diameter, for example, $R = 4.5 \text{ cm}$ and $H = 27 \text{ cm}$ are typical parameters. In order to find the optimal layout of cavities given this volume, several aspects must be considered. For now, we discuss only two cases. The first is a cylindrical cavity that fills the full volume. In this case, the angular average of the

coupling coefficient to a cross-polarized gravitational wave for the dominant TM_{010} mode (operating at 2.55 GHz) is $C_{\text{cyl}}^{\times} \approx 0.05$. The second case is that of N spherical cavities in the same magnetic volume, operated simultaneously, where at most $N = H/(2R)$, cavities can be placed. With $R = 4.5$ cm, there are three degenerate dominant modes TM_{m11} at frequency 2.91 GHz for $m \in \{-1, 0, 1\}$, with a combined average coupling coefficient of $C_{\text{sph}}^{\times} \approx 0.20$. As detailed in Sec. 4, the signal-to-noise ratio (SNR) for GW signals scales as the number N of simultaneously operated and coherently read out cavities. Comparing the two cases,

$$r \equiv \frac{\text{SNR}_{\text{cyl}}}{\text{SNR}_{\text{sph}}} \approx \left(\frac{\pi R^2 H}{4/3\pi R^3} \right) \cdot \frac{1}{N} \cdot \frac{C_{\text{cyl}}^{\times}}{C_{\text{sph}}^{\times}} = \left(\frac{H}{4/3R} \right) \cdot \frac{2R}{H} \cdot \frac{C_{\text{cyl}}^{\times}}{C_{\text{sph}}^{\times}} \approx \frac{3}{2} \cdot \frac{C_{\text{cyl}}^{\times}}{C_{\text{sph}}^{\times}} \approx 0.38,$$

however the coupling for cylindrical cavities is the lowest for large $H/(2R)$, as seen in Table 3. Instead, taking three cylindrical cavities with height $H = 9.0$ cm and radius $R = 4.5$ cm, for which $C_{\text{cyl}}^{\times} \approx 0.12$, reduces the SNR ratio to only $r = 0.90$, so, generally, to maximize the average coupling to the dominant mode, it is best to avoid high $H/(2R)$ cylindrical cavities. Hence, it is advantageous to operate multiple cavities with an aspect ratio closer to unity compared to one elongated cavity. However, coherently adding the contributions from multiple cavities presents an additional experimental challenge.

We recognize that the SNR also depends on the operating frequency f and the quality factor Q_0 of the cavity. Typically for a cylindrical cavity, the frequency will scale with height H , however, it is height independent for the mode TM_{010} . Because of this, and a similarity in frequency between the two compared cavity types, we only consider purely geometric factors for this estimate. A simulation comparing the intrinsic quality factor of a spherical and cylindrical cavities with radius $R = 4.3$ cm and height of $H = 9.0$ cm reveals a 27% higher Q_0 of the spherical cavity compared to the cylindrical one, assuming the same conductivity of 4×10^9 S/m corresponding to OFHC copper. This increases the SNR ratio in favor of spherical cavities to $r = 0.71$.

As discussed in Sec. 2.3, the response of a resonant cavity to HFGWs depends on the cavity quality factor Q as well as all the different modes that may be excited and the time dependence of the signal. Increasing Q simultaneously enhances the on-resonance signal power and narrows the resonance bandwidth, thus increasing the number of scan steps needed to cover a certain frequency interval. For a stationary monochromatic signal, assuming a fixed measurement time, this leads to a linear dependence of the SNR with the loaded cavity quality factor Q_l in case $Q_l \ll Q_s$, where Q_s is the effective quality factor of the GW signal. In this regime, the cavity bandwidth limits the measurement. If instead $Q_l \gg Q_s$, the SNR scales proportionally to $\sqrt{Q_l}$ because the signal power grows $\propto Q_l$ while the integrated noise decreases as $1/\sqrt{Q_l}$ [49]. In the special case $Q_l \sim Q_s$, one obtains the scaling $\text{SNR} \propto Q_l \sqrt{Q_s} \sim Q^{3/2}$. For transient HFGW signals considered with durations shorter than or comparable to the cavity ring-up time, the relevant observable is the total energy deposited in the cavity rather than the steady-state power. The deposited signal energy integrated over the signal duration is, to a good approximation, independent of Q_l as can be seen in equation (6), assuming that the readout time matches the signal duration given by $t_s = \Delta\nu/\dot{f} = f_0/(Q_l \dot{f})$. Considering the time integral over the noise power as $N = 2\Delta\nu t$ independent measurements of band-limited white noise the variance of the accumulated energy becomes $\text{Var}(E) = 2\langle E \rangle^2 / N = (k_B T)^2 \Delta\nu t$. Hence, the SNR scales as $E/\sigma_E \propto Q$. If the cavity fully rings up and the signal duration is longer than the readout (integration) time, the steady state case is recovered. In any case, a large unloaded quality factor Q_0 and therefore low losses in the cavity itself are always beneficial.

Simple high-frequency cavities can be milled into a block of solid copper, yielding unloaded Q -factors on the order of $5 - 10 \times 10^4$ [50]. There are two promising avenues for enhancing the quality factor of a cavity: coating the inner surface with a superconductor is the first approach, with an expected enhancement of the quality factor by a factor 10 to 1000. Characterizations of niobium–titanium, niobium–tin and rare-earth barium copper oxide (ReBCO) cavities in a strong magnetic field have already been conducted [51, 52]. Moreover, first successfully operated ultra-high Q cavities using ReBCO in strong magnetic fields have been already demonstrated at the Center for Axion and Precision Physics Research (CAPP) [53, 54]. Moreover, tests using niobium nitride coating (Figure 5) were also reported in [55]. The second approach targets the use of dielectric cavities, which have shown an enhancement of Q by a factor of 10^3 over superconducting cavities in strong magnetic fields, at the cost of a smaller effective volume for the cavity mode [53, 56]. While ReBCO and dielectric cavities can already be used for HFGWs searches, they apply only to cylindrical cavities, due to the nature of these materials. Fabrication of cavities with more complex geometries, such as spherical cavities, requires a different deposition technique, such as sputtering. Besides, the position of the antennas within the cavities must be optimized. Overall, it seems that quality factors on the order of 5×10^5 are reachable.

Another interesting venue for cavity optimization is the use of metamaterials to artificially change the plasma frequency of the cavity which modifies the relation between the geometry of the cavity and its resonance frequencies. This can be achieved, for example, by filling the cavity volume with a regular grid of wires. Changing the distances of the wires changes the resonance frequency while the effective volume remains constant. This is in particular

interesting for higher frequencies, where usually the cavity volume becomes rather small. This approach, also known as *plasma haloscope* has been studied recently in [57–60] and in particular in the context of GW searches in [58].

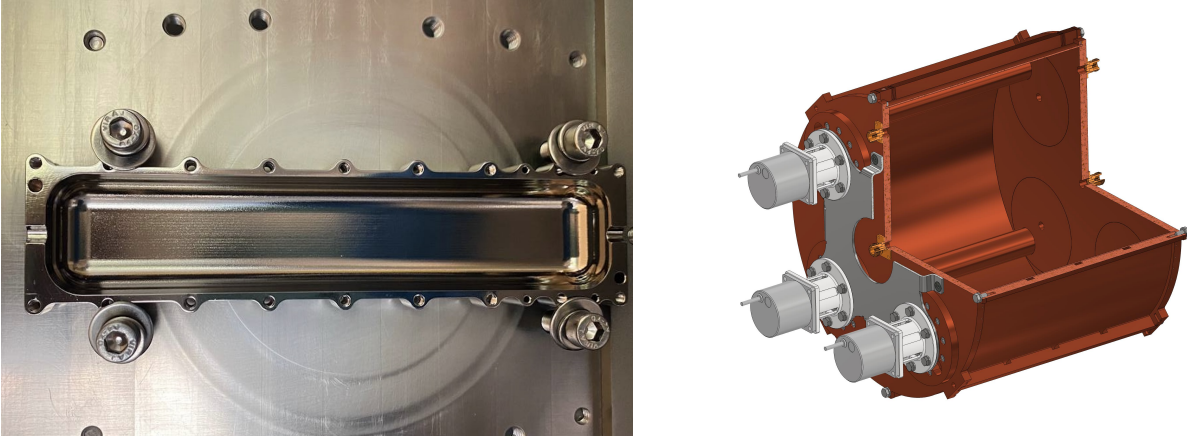


Fig. 5. Left: NbN coated cavity studied in the Supax setup in [55]. Right: schematic drawing of the FLASH cavity prototype (1/6 scale compared to the original).

3.3 Basic Cavity Readout Systems

The simplest readout scheme of a typical cavity-based axion-search experiment — and for this matter also for HFGW experiments — is based on a real-time spectrum analyzer that is capable of streaming in-phase and quadrature (IQ) time-series data to a readout computer. This approach is limited by intrinsic (e.g. thermal and electronic) noise, however, is simple to realize and builds therefore the baseline to which we compare the advanced readout schemes in the following.

The optimal linear amplifiers are based on quantum technologies. Their intrinsic noise is due to quantum fluctuations of the signal whose minimum value at the input of the amplifier is bounded to twice the zero-point energy for the mode ω of interest, $\hbar\omega/2$, and is usually expressed as an effective temperature $T_{\text{SQL}} = \hbar\omega/k_B$. The contribution to the noise power is then $P_{\text{SQL}} = \hbar\omega\sqrt{\Delta\nu/t}$ [61, 62], where $\Delta\nu$ is the signal bandwidth which corresponds to the cavity bandwidth b for transient signals and t the acquisition time. Different types of quantum amplifiers are used for axion experiments as well as superconducting-qubit readout [63]. It is also a well-established technology that is commercially available. Depending on the frequency range and bandwidth, three different types of amplifiers can be distinguished: Microstrip Superconducting Quantum Interference Device (MS SQUID), Josephson Parametric Amplifiers (JPAs), and Superconducting Travelling Wave Amplifiers (TWPAs) [64–66]. We foresee using a SQUID for the readout of the FLASH cavity and TWPA and JPA amplifiers for the small GHz cavities. For the latter, we also investigate the single-photon-detection approach.

An overview of expected noise power for the different readout technologies vs. the cavity resonance frequency is shown in Figure 6 where: the r.m.s of the thermal power from a resonator of quality factor Q_l is

$$\sigma_{\bar{P}_{\text{th}}} = \frac{\sigma_{E_{\text{tot}}}}{t} = hf\sqrt{n(T)(n(T)+1)}\sqrt{\frac{f}{Q_l t}}, \quad (10)$$

where h is the Planck constant, f is the photon frequency, and $n(T)$ is the photon occupation number in the cavity at temperature T . The standard quantum limit (SQL) of an amplifier, that includes amplifier added noise and vacuum fluctuations, is $P_{\text{SQL}} = hf\sqrt{f/Q_l t}$; the noise $P_{\text{dark counts}} = hf\sqrt{\nu_{\text{DC}}/t}$ where ν_{DC} is the device dark count rate [67].

3.4 Multimode Readout Development for the MHz Cavities

HFGWs couple to TM and TE modes with similar strength. Depending on their polarization, we will acquire both types of modes from the FLASH cavity in the frequency range between 100 and 300 MHz. Two distinct antennas

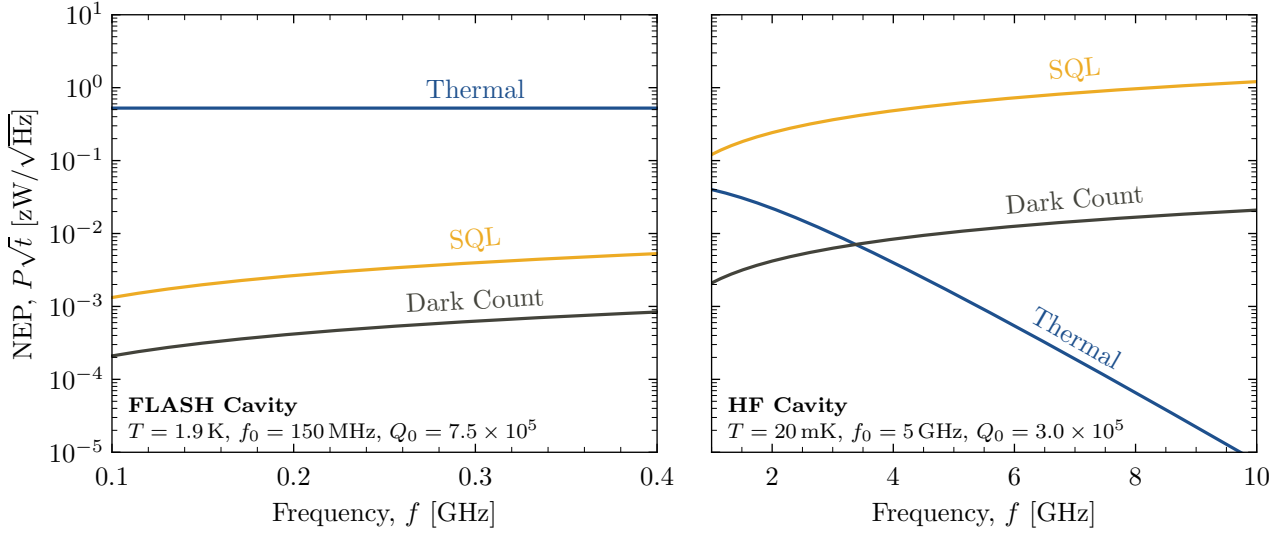


Fig. 6. The noise equivalent power (NEP) with frequency f for the dominant noise contributions: thermal noise, dark count (using a dark count rate of 10 Hz), and quantum noise at the standard quantum limit (SQL). These are computed by dividing the relevant noise power by the frequency resolution, equivalent to $P\sqrt{t}$, where t is the total integration time. **Left:** The noise spectral density for the FLASH cavity system. **Right:** The noise spectral density for the high-frequency (HF) cavity system. Both of these configurations are summarised in Tab. 4.

will couple to TM and TE modes, a dipole and a loop antenna, respectively. A Microstrip SQUID Amplifier (MSA) [64, 68] kept at 1.9 K is expected to be an optimal solution with a noise added by the amplifier between 200 and 400 mK, in terms of low noise, frequency band and gain, for the first stage of signal amplification. As second amplification stage a cryogenic heterojunction field-effect transistor (HFET) amplifier will be employed. The signal will be split at room temperature and bandpass filters will select the modes of interest before digitization. Multichannel fast ADCs together with FPGA based signal processing will be used to acquire the signals. The offline combination of five modes with a 2σ threshold will allow, for instance, a background reduction by 9 orders of magnitude, sufficient to detect transient events. Preliminary studies on this readout scheme have been already successfully conducted [46]. In summary, we expect a noise level of $T_{\text{sys}} = 2.2 \text{ K}$ in the final readout system.

3.5 Multimode Readout Development for GHz Cavities

Microstrip SQUID amplifiers are well suited for readout at frequencies up to approximately 1 GHz. In this regime, their noise performance is dominated by dissipation in the shunt resistors required for stable SQUID operation, which prevents them from reaching the quantum limit but still allows for near-quantum-limited amplification with excellent linearity and dynamic range [64]. However, at higher resonance frequencies, the noise performance of SQUID-based amplifiers degrades, and alternative technologies are required.

For cavities operating at several GHz, Josephson parametric amplifiers (JPAs) and travelling-wave parametric amplifiers (TWPAs) constitute promising alternatives. JPAs [65] can operate at the quantum limit and are frequency tunable, but they typically provide only narrow instantaneous bandwidths (of order tens of MHz), making them less suitable for simultaneous readout of multiple cavity modes. In contrast, TWPAs [66] operate efficiently at frequencies above approximately 4 GHz and offer significantly larger bandwidths in the GHz regime, ranging from about 1 GHz for four-wave-mixing designs up to roughly 4 GHz for three-wave-mixing implementations. This wide bandwidth makes TWPAs particularly attractive for multimode or multiplexed readout schemes relevant for GRAVNET. Their main drawback is a higher added noise compared to JPAs, typically corresponding to a noise temperature of a few $\hbar\omega/k_B$.

In practice, several readout architectures are conceivable. Signals from different cavity resonances may be frequency-multiplexed and amplified by multiple JPAs, or alternatively amplified simultaneously using a single broadband TWPA. While the detailed design of the readout chain remains to be optimized, initial studies—based,

for example, on Ref. [69]—indicate that a total system noise temperature of $T_{\text{sys}} \simeq 300$ mK is achievable for GHz-frequency cavities.

3.6 Single-Photon-Counting Readout

At frequencies above a few GHz the quantum noise $\hbar\omega$, rising linearly with frequency, spoils the benefits of working with a dilution refrigerator. To get around this limit, a considerable effort is ongoing to exploit quantum techniques such as squeezing, quantum metrology, and quantum sensing to achieve optimal measurement strategies for axion-dark-matter searches [70–72]. It is therefore the aim to develop dedicated single-photon quantum sensors with a detection efficiency higher than 50% for photons with frequency between 1 and 10 GHz, with a dark-count rate of less than a few Hz, so that the contribution given to noise is less than the thermal one.

Single-photon detection at microwave frequencies with circuits based on superconducting transmon qubits [73] was achieved in 2007 [74]. We already successfully performed qubit spectroscopy and quantum sensing experiments [75–80]. Of interest for cavity experiments operating at large magnetic field is the itinerant photon detection, that allows keeping the superconducting electronics away from the \vec{B} -field region. Several experimental schemes for itinerant photons, based on superconducting qubits, have been proposed and realized [79–84], but still with dark-count rates larger than 100 Hz. Alternatively, the development of a magnetic field resistant qubit [78] would be a game changer enabling the possibility to adopt quantum non demolition (QND) schemes as well as searches through direct qubit excitation [85]. QND measurements enable repeated measurement of the presence of a single photon, opening up the way to error corrections and to drastic reduction in dark-count rates. QND measurements have been successfully used for the detection of photons generated inside a cavity [86]. Within GRAVNET, we propose an extension to two qubits of the scheme in [84], where a controlled Z-gate⁵ between an incoming itinerant photon and a transmon qubit mounted inside a resonator was used to detect the photon arrival and reflection [77]. In this new scheme, the dark-count rate scales with $p(1|0)^2$ instead of linearly, where $p(1|0)$ is the probability of erroneously measuring the qubit state 1 when it is 0. As $p(1|0)$ can be as low as 0.1%, this corresponds to a reduction in dark counts by up to three orders of magnitude. The minimum sensitivity reachable by this scheme for the amplitude of a coherent signal generated for a time duration t_{signal} is on the order of

$$\bar{n}_{\text{min}} = 1/N_{\text{measure}} = \tau_{\text{measure}}/t_{\text{signal}}, \quad (11)$$

where N_{measure} is the number of repeated measurements in a time t_{signal} and τ_{measure} is the single measurement duration. In this scheme $\tau_{\text{measure}} \sim 1/\gamma_{\text{cavity}}$, where γ_{cavity} is the bandwidth of the conversion cavity, so that the integrated probability to produce a photon is

$$\int \dot{n} dt \sim \gamma_{\text{cavity}} \bar{n} t_{\text{signal}} \sim 1. \quad (12)$$

Given the quasi non-demolition nature of the measurement, probing successively and repeatedly with N_q qubit-sensors the same coherent state would lead a factor $\int \dot{n} dt \sim 1/N_q$ below the single photon sensitivity. Entanglement of two or more qubits, such as the Greenberger–Horne–Zeilinger $|GHZ\rangle = (|000\dots 000\rangle + |111\dots 111\rangle)$ state [87], will be considered to further improve the sensitivity, although it is known that these states are very weak and subject to decoherence. Further enhancement of the sensitivity to strain, can be obtained by injecting squeezed-vacuum states into the resonant cavity as in [88]. The ultimate sensitivity might be obtained by combining squeezing and photodetection as discussed in [71, 72].

It is illustrative to discuss the single photon counting with a concrete example. For a cavity with a resonance frequency of 5 GHz, the corresponding photon energy is $E_\gamma \approx 3.3 \times 10^{-24}$ J = 2×10^{-5} eV. In a naive picture, this is the minimal energy that must be deposited in the cavity to create at least one photon. However, photon creation is a quantum mechanical process, where the likelihood for a single-photon creation is following a Poisson distribution with mean $\lambda = E_{\text{HFGW}}/E_\gamma$, where E_{HFGW} is the deposited energy of the HFGW. Hence, even tiny deposited energies that are smaller than the single photon energy could yield real photons, however, linearly suppressed with λ .

4 Network Operation

The numerous advantages of detector networks in the context of fundamental physics have been convincingly demonstrated not only for gravitational-wave detection (LIGO–Virgo–Kagra [89]), but also for various families

⁵ A change of sign of the qubit state $|1\rangle$ controlled by the arrival of a single photon

of dark-matter detectors, starting from the global network of optical magnetometers for exotic physics searches (GNOME [90, 91]), atomic-clock networks such as GPS.DM [92], as well as currently emerging multi-sensor networks [91] based on diverse sensors such as atomic spectrometers designed to detect fast (up to 100 MHz) oscillations of fundamental constants [93] and ferromagnetic detectors of galactic axion-like particles (SHAFT [94]).

For the initial version of GRAVNET, we foresee operation with a large cavity at the FLASH magnet as well as nine small-scale cavities at the laboratories in Bonn, Frascati and Mainz, where three cavities are operated together in identical setups at each site. In the following discussion, we consider combining the signals of the nine GHz cavities, operating at similar frequencies around 6 GHz. Two further simplifications are made: first, we ignore the fact that higher modes can be additionally read out for each cavity, which would yield additional information and hence increase the sensitivity. Second, we ignore the timing difference of incoming signals at the three network nodes, which depends on the location of the HFGW source and can range between 0 and ≈ 3 ms.

Operating multiple HFGW detectors as a network provides a robust way to enhance sensitivity, reject instrumental backgrounds, and extract signal coherence. We discuss how the signal-to-noise ratio (SNR) scales with the number of detectors N_{cav} , distinguishing between two detection strategies: continuous power readout and single-photon counting. The scaling depends critically on whether the signal is combined coherently or incoherently and on the statistical nature of the dominant noise. In this work, we distinguish between the intrinsic SNR used in spectral analyses from correlation detection strategies. For a network of N_{cav} detectors linked incoherently, the intrinsic SNR scales at most as $\sqrt{N_{\text{cav}}}$, while in the ideal case of a coherent combination it scales linearly with N_{cav} . The detector network provides further advantages from correlation strategies, in which each detector scans a time window ΔT for discrete candidates. In this case, increasing the number of detectors leads to a strong suppression of the false alarm probability for a fixed intrinsic SNR.

In a power readout scheme the measured output of the i -th detector may be written as $P_i(t) = P_{\text{sig}}(t) + n_i(t)$, where $P_{\text{sig}}(t)$ denotes the signal contribution and $n_i(t)$ represents stochastic noise, assumed to be uncorrelated between different detectors. If the detector outputs are combined incoherently at the power level, the total signal scales linearly with the number of detectors, while the noise adds in quadrature. The resulting network SNR therefore scales as $\text{SNR}_{\text{net}} = \sqrt{N_{\text{cav}}} \cdot \text{SNR}_{\text{single}}$. If, on the other hand, the signal phase information is preserved and the detector outputs can be combined coherently, the signal amplitudes add linearly while the noise remains incoherent. In this optimal case, the network SNR scales as $\text{SNR}_{\text{net}} = N_{\text{cav}} \cdot \text{SNR}_{\text{single}}$. Achieving this scaling requires precise relative timing and phase calibration between detectors, as well as a sufficient signal coherence time.

The situation changes when considering a single-photon readout in each cavity. Here, the crucial aspect is the dark-count rate, or background rate of single-photon detection per time step Δt . For a single detector, the expected number of signal and background counts are denoted by μ_{sig} and μ_{bkg} , respectively, and are assumed to follow Poisson statistics. For a network of N_{cav} independent detectors, the total expected signal count scales as

$$\mu_{\text{sig}}^{\text{net}} = N_{\text{cav}} \mu_{\text{sig}}, \quad (13)$$

while the statistical uncertainty is dominated by background fluctuations,

$$\sigma_{\text{net}} = \sqrt{N_{\text{cav}} \mu_{\text{bkg}}}. \quad (14)$$

The resulting network SNR is therefore given by

$$\text{SNR}_{\text{net}} = \frac{N_{\text{cav}} \mu_{\text{sig}}}{\sqrt{N_{\text{cav}} \mu_{\text{bkg}}}} = \sqrt{N_{\text{cav}}} \text{SNR}_{\text{single}}. \quad (15)$$

Because photon counting is intrinsically incoherent, this $\sqrt{N_{\text{cav}}}$ scaling represents the optimal sensitivity improvement achievable by increasing the number of detectors. For transient signals, additional discrimination against background can be achieved by requiring temporal coincidence between photon detection events in multiple detectors. Coincidence requirements significantly suppress false-positive rates by reducing the effective background, thereby enhancing detection confidence.

Consider a network of N_{cav} single-photon detectors, each operated in independent measurement windows of duration Δt . Let p_{sig} be the probability for a detector to register a signal photon if a GW is present, and p_{bkg} the probability for a background (noise) count, per measurement window. A k -fold coincidence is defined as the detection of photons in at least k out of N_{cav} detectors within the same measurement window. For arbitrary p_{sig} , the probability for a k -fold coincidence in a single measurement window is given by the binomial sum

$$p_{\text{sig}}^{(k)} = \sum_{j=k}^N \binom{N}{j} (p_{\text{sig}})^j (1 - p_{\text{sig}})^{N-j}, \quad (16)$$

and similarly for accidental coincidences due to noise,

$$p_{\text{bkg}}^{(k)} = \sum_{j=k}^N \binom{N}{j} (p_{\text{bkg}})^j (1 - p_{\text{bkg}})^{N-j}. \quad (17)$$

In the limit of rare events, $p_{\text{bkg}} \ll 1$, these reduce to the familiar approximation

$$p_{\text{bkg}}^{(k)} \simeq \binom{N}{k} (p_{\text{bkg}})^k. \quad (18)$$

Over N_t independent measurement windows, the expected number of background coincidences is $\mu_{\text{bkg}} = N_t p_{\text{bkg}}^{(k)}$. With one GW event per year, the expected number of detected signal coincidences scales as $\mu_{\text{sig}} = 1 \cdot p_{\text{sig}}^{(k)}$.

Assuming Poisson statistics for the background, the standard deviation of background coincidences is

$$\text{SNR}_{\text{net}} = \frac{\mu_{\text{sig}}}{\sqrt{\mu_{\text{bkg}}}} = \frac{p_{\text{sig}}^{(k)}}{\sqrt{N_t p_{\text{bkg}}^{(k)}}}. \quad (19)$$

In the rare-event limit $p_{\text{bkg}} \ll 1$ and $p_{\text{sig}} \approx \mathcal{O}(1)$, one can approximate

$$\text{SNR}_{\text{net}} \simeq \frac{1}{\sqrt{N_t \binom{N_{\text{cav}}}{k}}} \frac{p_{\text{sig}}^{(k)}}{p_{\text{bkg}}^{k/2}}. \quad (20)$$

This shows that increasing the number of detectors strongly enhances the SNR: for linearly increasing coincidence order k , alongside n (fixed $n - k$ term), as long as $p_{\text{sig}} \gg p_{\text{bkg}}$, we expect an exponential increase in the signal to noise ratio. For larger signal probabilities, the exact binomial sum must be used, and the SNR scaling with N_{cav} eventually saturates as the coincidence probability approaches unity.

In short, for both scenarios, the network operation will boost the statistical sensitivity and allows for a much better control of systematics and rejection of false signals. Examples are given in Sec. 6.3. For network synchronization, each experimental site will be equipped with a GPS-referenced data-acquisition system offering several channels of analog-to-digit converters (ADC), several digital channels, and GPS-based time synchronization at a level of better than 200 ns.

The key decision to be made (see below) is how much of the raw data needs to be stored and transferred versus ‘smart pre-processing’ of the raw data (which could reduce the amount of ‘byte trafficking’ by many orders of magnitude at the expense of limiting the opportunities for post-processing raw data).

4.1 Triggering and Data Transfer

In the case of a single-photon readout, the expected data rate per cavity will be minimal and corresponds to the background or noise rate of the system. The situation is significantly different for a continuous readout scheme, where the voltage $V(t)$ needs to be recorded for each cavity. The expected raw data rate per cavity depends on the digitized bandwidth, precision of the digitized values, and the number of modes to be read out. Typically 14 bits per value are used and a bandwidth of several MHz, yielding data rates of tens to hundreds of MB/s. This would be necessary to both coherently add the signal across the entire network and thus optimize the SNR. The data volume per site that hosts three cavities could therefore accumulate to several tens of TB per day, requiring a stable high-speed connection to the other participating institutions. Hence a dedicated online analysis system has to be developed which analyses the recorded data instantaneously and only keeps such information, where local upwards fluctuations are present. The relevant time-steps are marked and sent to all other participating sites, so that the corresponding information is kept also at their locations for further analysis. We expect to reduce the necessary data-transfer across all sites by at least a factor of 20. In a common data-center, a combined analysis will then be performed on a daily basis, and only the potentially interesting data blocks will be retained. In addition, it is foreseen to implement a random trigger, which keeps around 2% of the data on each site in addition to the signal-triggered events. With this approach, we expect to reduce the overall data volume stored per site and per day of data taking to at most 1 TB.

5 Analysis Considerations

A diverse network of GW detectors offers a multitude of analysis possibilities, where the analysis approach depends not only on the targeted signal source (transient or monochromatic), but also on the detector technologies employed within the network which could resolve the time-structure of the signal, e.g. using a time-resolved power measurement or only detect the presence of a signal, and could be sensitive at similar frequencies or cover a larger span of frequencies.

In the initial phase of GRAVNET each detector is responsible for analysing its data stream in real time and flag time periods containing a potential signal. This 'trigger' signal is distributed among all active detectors in the network, which will then save the raw detector data within the time-span in question to facilitate a combined analysis at a later stage. The stored time-window takes into account the spatial distance of the detectors of 200 to several thousand kilometers, leading to significant shifts in arrival time of the signal of up to 40 ms which are potentially longer than the duration of a transient signal.

The most simple combination of data from different network sites is a coincidence analysis, which only requires a yes/no decision from each detector and allows the combination of arbitrary detector technologies. The general principle is discussed in Sec. 4 and sensitivity estimates are given in Sec. 6.2. For transient events, the direction of the source can be located by measuring the relative differences of the arrival time of the signal if at least four stations measure a signal.

If the time-evolution of the GW signal can be measured, more advanced combinations of the time-series data can be imagined, similar to what current GW observatories do. This would allow for a more precise determination of the source position, as well as deducing insights on the parameters of the signal source.

Real-time analysis of detector data largely depends on the detector technology used. If the GW waveform is reconstructed, e.g. in the case of a classic power readout, the signal can be recovered from the detector and thermal noise by means of matched filtering or machine learning approximation of optimal filter. A yes/no decision on the presence of a signal could be taken e.g. utilizing modern methods of anomaly detection like variational autoencoders. If multiple detectors, e.g. multiple cavities or the readout of multiple cavity modes from the same cavity, are used at one site, the signals could be added coherently if the frequencies are identical or combined in a search for transient signals locally to reduce the background rate.

If more sensitive technologies like single photons counting or other quantum metrology methods are used the information on the waveform of the signal is typically lost. Those detectors require specific readout protocols that vary depending on the detector technology and are not discussed in detail here. The output is always a yes/no decision on a potential signal photon, and the state of many such detectors can easily be combined in a coincidence-type experiment, as mentioned above.

In the next chapter, sensitivity prospects are presented for some individual detectors using RF cavities with classic power detection and single photon counting, as well as the impact of the combination of signals in a coincidence style experiment.

6 Performance of GravNet

As an example case, we discuss the sensitivity of GRAVNET to transient gravitational wave signals from PBH mergers with masses between 10^{-7} and $10^{-16} M_{\odot}$, where we estimate the maximal distance from Earth of those merger events that are still detectable with our terrestrial experiment. This can be converted to an upper limit on the density of primordial black holes in our galaxy, assuming, in addition, a certain length of data taking, which we take to be one year in the following. The preliminary estimates presented in the following should give the reader an idea of the achievable sensitivity.

In Sections 6.1 and 6.3 the sensitivities achievable with a single cavity are discussed using power readout with parametric amplification and advanced readout techniques employing single-photon counters, respectively. The combination of different detectors at different locations is discussed in Section 6.2.

6.1 Expected sensitivities of a baseline system of GravNet

In the baseline GRAVNET system, we foresee operation of the sub-gigahertz FLASH Cavity at a temperature of 1.9 K, while nine gigahertz-range cavities will be operated simultaneously at $T = 20$ mK. We expect achieving quality factors of $Q_0^{\text{LF}} = 7.5 \times 10^5$ and $Q_0^{\text{HF}} = 3 \times 10^5$ in the large and small cavities, respectively. Targeting an antenna coupling factor of $\beta = 1$ when operating at fixed frequencies, the loaded quality factor will be $Q_l = 0.5 Q_0$.

The readout system for all cavities in the baseline version of GRAVNET will be realized with parametric amplifiers as the first stage, either JPAs or TWPAs, yielding, in both cases, a system noise temperature about $T_{\text{sys}} = 300$ mK for the high-frequency setups. The low-frequency setup is dominated by the 1.9 K thermal noise, which yields a system noise temperature about 2.2 K adding 0.3 K from the SQUID amplifier. The SNR is calculated using the approach to evaluating the RF power generated in the cavity discussed in Section 2.3, in particular, Eq. 7. The noise power depending on the system noise temperature is calculated as

$$P_{\text{noise}} = k_B T_{\text{sys}} \Delta\nu, \quad (21)$$

where $\Delta\nu$ integrated bandwidth of the readout, taken to be 10 kHz in the HF setup and 200 Hz in the FLASH setup. The resulting noise power is shown in Tab. 4.

Setup	f_0 [GHz]	Q_0	T_{sys} [K]	P_{noise} [W]	h^{min}
HF	5.0	3.0×10^5	0.3	4×10^{-20}	1.7×10^{-20}
FLASH	0.15	7.5×10^5	2.2	6×10^{-21}	2.2×10^{-21}

Table 4. Noise power for different cavity setups and the corresponding strain sensitivity assuming $\text{SNR} = 0.08$ (see text). For the HF cavity the amplifier noise is the dominating noise source whereas for the FLASH cavity the 1.9 K black-body radiation of the cavity itself is the dominant noise source.

The minimally detectable signal is given by the SNR required for detection at a given confidence level. Assuming a measurement time of one year with order 10^{10} measurement intervals and less than one false positive signal within the measurement period leads to a false positive rate (FPR) for an individual measurement of $< 10^{-10}$ which corresponds to a threshold of 6.36σ above the noise. This translates into a required SNR of 8, if the confidence level of a positive signal is set to 95% using $\text{SNR} = \Theta + \Phi^{-1}(c_1)$, where c_1 is the desired confidence level, Φ^{-1} is the inverse of the cumulative distribution function of the normal distribution, and Θ is the threshold in sigmas of a normal distribution corresponding to the desired false positive rate. Note that for different signal-duration assumptions, the readout window is adjusted accordingly to optimize sensitivity. This can quickly lead to tightened requirements on the FPR rate to 10^{-12} , only slightly increasing the threshold to 7σ and hence the required SNR to 8.6. The needed power for a positive identification of a signal is drastically reduced if the (known) shape of the signal in the time-domain is exploited by means of matched filtering. This enhances the SNR at a given signal power by up to a factor of 100 [95] under ideal conditions. Hence, the needed maximum signal power is taken to be $0.08 P_{\text{noise}}$. The resulting minimally detectable strain h^{min} is calculated using Eq. 7 and the cavity properties described in Sec. 3.2 and presented in Tab. 4.

In this setup, the strain sensitivity is largely independent of the duration of the signal and hence the PBH mass as long as the cavity is fully rung up. The reason is that the the voltage in the cavity is proportional to the strain of the signal which scales with $M_{\text{PBH}}^{5/3}$ while the time the signal spends within the bandwidth of the cavity scales inversely with $t \propto 1/\dot{f} \propto 1/M_{\text{PBH}}^{5/3}$ and the SNR gain of the matched filter is proportional to the time of the signal [96]. Hence, it is most instructive to show the reach in distance for a given PBH mass, which is displayed in Figure 7. For very fast transient signals the cavity may not be fully rung up. This is modeled by using an effective quality factor for the cavity defined as $Q_{\text{eff}} = \min(Q_l, N_{\text{cyc}})$, where N_{cyc} is the number of cycles the signal spends within the bandwidth of the cavity. With only a few photons produced in the cavity, the power readout scheme fails and one must turn to advanced techniques like single photon detection. These are discussed in Sec. 6.3.

Using a resonant structure in the experiment yields the best sensitivity close to the resonance frequency f_0 , outside of which the resonant enhancement drops like $1/(f_0 - f)^2$. Even considering that the signal power induced by the GW rises proportional to the frequency of the gravitational wave ω_g , see Eq. 7, the sensitivity drops quickly when moving away from the resonance frequency. In the intermediate frequency range, one typically finds a multitude of higher order resonant modes which can be exploited to achieve sensitivity at several frequencies simultaneously with a single cavity. The gain in sensitivity to transient signals will be studied in future work.

6.2 Network operation

In this section, we illustrate the implications of the network formalism discussed above by considering concrete benchmark scenarios. We focus on transient HFGW signals and assume an expected event rate of order one

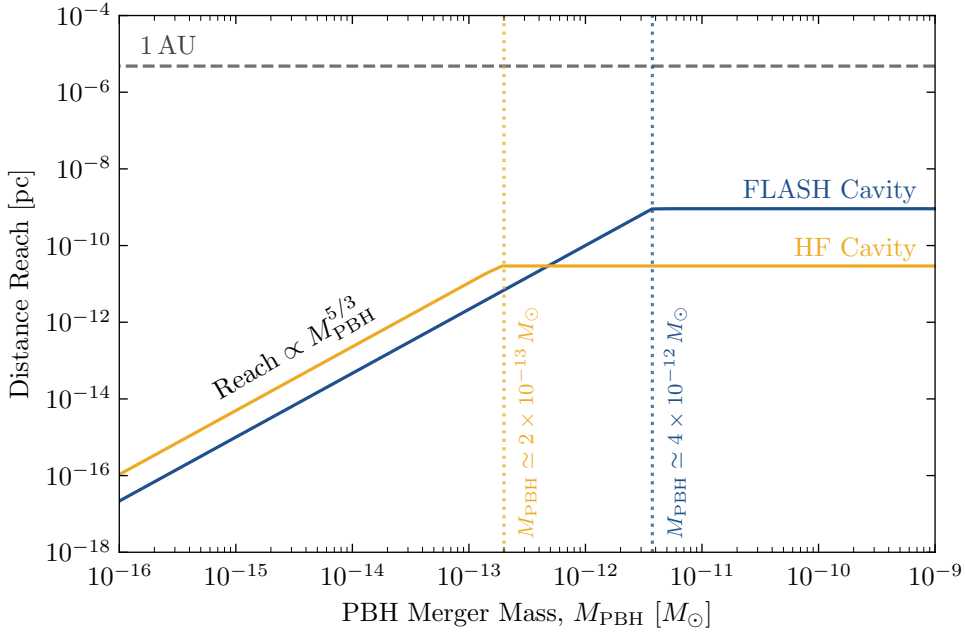


Fig. 7. The distance reach for observing a PBH merger event at a given PBH merger mass M_{PBH} at a 95% confidence level and a false positive rate below 10^{-10} . This requires an SNR of at least 0.08 assuming a linear readout of the cavity signals. Larger PBH masses lead to faster transient signals, which eventually cannot fully ring up the cavity. At this point, the distance reach becomes constant, occurring at the PBH merger masses indicated by the vertical lines. Also marked is $1 \text{ AU} \simeq 4.8 \times 10^{-6} \text{ pc}$.

detectable signal per year traversing the detector network located at Bonn, Mainz, and Frascati. Any impact due to the detector orientation is negligible, as can be seen from Fig. 2 as the angular separation is at most 9° .

We denote by p_{sig} the single-cavity detection efficiency, defined as the probability that a cavity registers a measurable response when an HFGW signal passes through the network. This efficiency is independent of the specific readout scheme (continuous power readout or single-photon counting), as it reflects the probability that a given signal strength produces a detectable response within a fixed time window. For the following examples, we assume a representative single-cavity detection efficiency of $p_{\text{sig}} = 0.9$, i.e. a HFGW crossing the network is detected with probability 0.9 in each cavity.

The background probability per cavity and per measurement window is denoted by p_{bkg} . We assume a measurement window of duration $\Delta t = 3 \text{ ms}$, corresponding to the characteristic time resolution discussed in Sec. 4. Over one year of operation, this yields $N_t = \frac{365 \times 24 \times 3600 \text{ s}}{\Delta t} \simeq 10^{10}$ independent measurement windows. In order to ensure robust detection, the expected number of accidental background coincidences over the full network and the full data-taking period must be well below unity. This motivates the use of coincidence measurements across multiple detectors.

As a first benchmark, we consider a network of $N = 9$ cavities operated in parallel and assume a background probability per cavity and per measurement window of $p_{\text{bkg}} = 0.03$. Using the coincidence formalism developed in Sec. 4, we evaluate the expected number of accidental coincidences as a function of the required coincidence order k . As shown in Figure 8 left, requiring a coincidence of at least $k = 8$ out of 9 detectors suppresses the expected number of background events to below 0.1 per year, while simultaneously retaining a high signal efficiency. In particular, the probability that a genuine HFGW signal produces a coincidence in at least 8 detectors exceeds 0.9 for the assumed single-cavity detection efficiency $p_{\text{sig}} = 0.9$.

A more challenging scenario is illustrated in Figure 8, right panel, where we assume a significantly larger background probability per site and per measurement window, $p_{\text{bkg}} = 0.15$. In this case, stronger combinatorial suppression is required to reduce the expected number of accidental coincidences below unity over the full data-taking period. As shown in Figure 8, this can be achieved by increasing both the network size and the coincidence requirement. Specifically, for a network of $N = 18$ cavities, requiring coincidences in at least $k = 16$ detectors suffices to suppress the background to an acceptable level while maintaining a high probability of detecting a true signal.

These examples illustrate a central feature of the GRAVNET concept: as long as the per-site background probability p_{bkg} is significantly smaller than the single-site detection efficiency p , accidental backgrounds can be

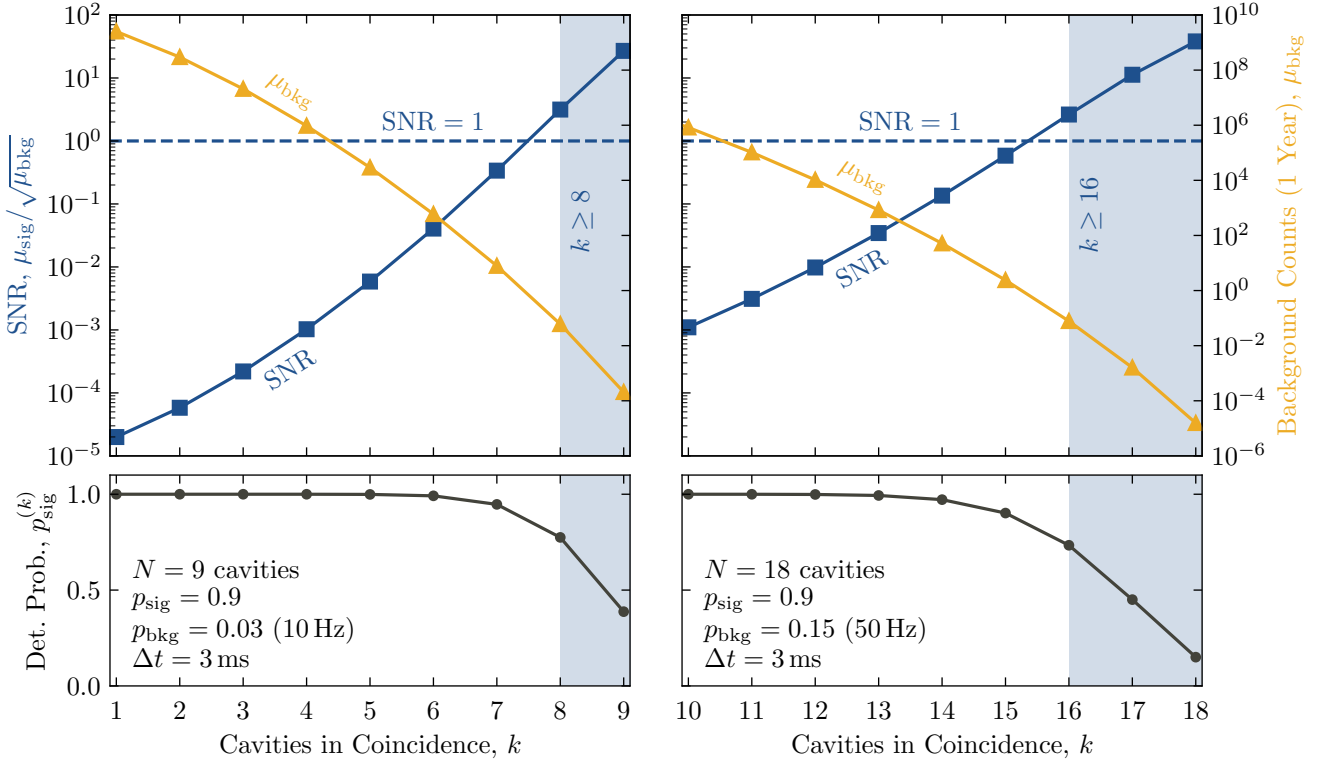


Fig. 8. Expected signal-to-noise ratio (SNR) and background performance over one year with required cavity coincidence order k for a network of cavities. Also shown are the probabilities to detect a true HFGW signal for a given coincidence order, $p_{\text{sig}}^{(k)}$. The assumed cavity detection efficiency is $p_{\text{sig}} = 0.9$ and the measurement window is taken to be $\Delta t = 3$ ms. **Left:** The performance of a network of $N = 9$ cavities with assumed background probability per cavity and per measurement window of $p_{\text{bkg}} = 0.03$. **Right:** The performance of a network of $N = 18$ cavities with assumed background probability per cavity and per measurement window of $p_{\text{bkg}} = 0.15$.

suppressed to arbitrarily low levels by increasing the number of detectors and imposing appropriate coincidence requirements. In contrast, the signal efficiency is fundamentally limited by the sensitivity of individual detectors.

Consequently, the primary experimental objective must be to maximize the single-cavity detection efficiency, i.e. to optimize the detector sensitivity to the smallest possible gravitational-wave strains. Network operation and coincidence analysis then provide a scalable and robust mechanism for background rejection, even in the presence of relatively large per-detector background rates.

6.3 Expected sensitivity for an advanced readout system and multiple detectors

In the long-term perspective, the high-frequency detectors of GRAVNET are envisioned to be equipped with single-photon detectors (SPDs) which are discussed in Sec. 3.6. In this configuration, the experiment becomes a counting experiment, in which the dominant background contributions arise from thermal photons in the cavity and from intrinsic dark counts of the SPDs. The background count rate of an individual detector is assumed to follow Poisson statistics, with a mean determined by the sum of all noise contributions and proportional to the duration of the detector readout window. The contribution from thermal (blackbody) radiation inside the cavity can be estimated from the corresponding black body radiation P_{bb} , multiplied with the antenna absorption [97]. At millikelvin temperatures and for GHz-scale frequencies, this thermal contribution is exponentially suppressed and remains negligible at the envisioned operating temperature of 20 mK compared to the zero-point energy of the cavity as shown in Fig. 6.

The signal threshold in number of photons N_{sig} is given by the allowed false positive rate, which is typically chosen to be one per year, and the number of measurement interval within this period. Typical measurement intervals for SPDs are on the order of milliseconds, yielding about 10^{10} measurement intervals per year. Correspondingly,

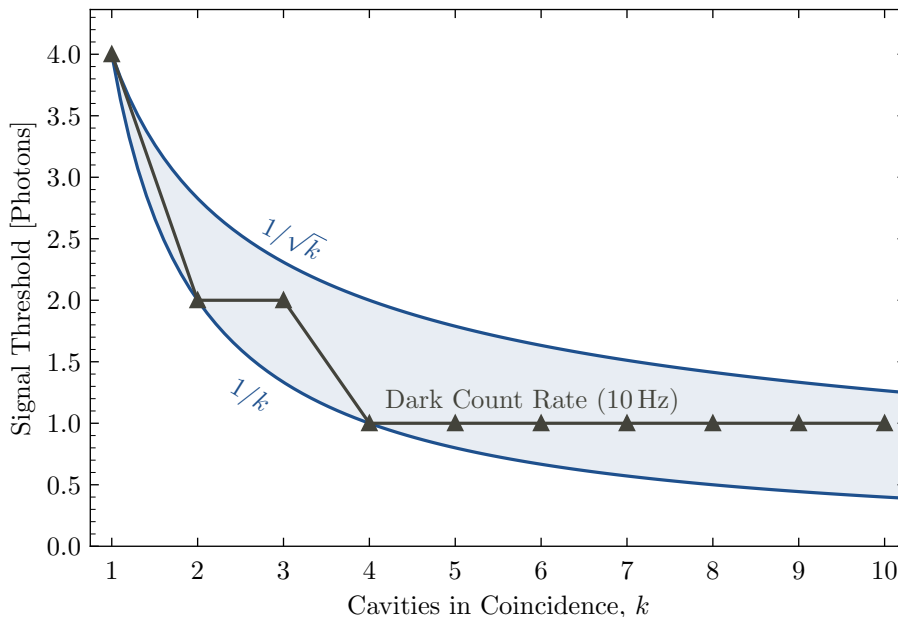


Fig. 9. Required minimum threshold of signal photons to achieve a false positive probability per measurement $< 10^{-10}$ as a function of the number of detectors in coincidence. An SPD dark count rate of 10 Hz is assumed to be the dominant noise source.

the probability of an accidental positive signal detection must be $< 10^{-10}$ per measurement. From this the signal threshold in number of photons N_{thr} is calculated using the inverse survival function of the Poisson distribution with a mean number of background events $\mu_{\text{bkg}} = P_{\text{noise}}$ and the target probability 10^{-10} . As an example, assuming a dark count rate of 10 Hz which is close to already achieved values [98], and consequently $P_{\text{noise}} = 0.01$, a signal threshold of $N_{\text{thr}} = 4$ photons is found. Operating multiple detectors in coincidence will drastically reduce the signal threshold, as shown in Sec. 4. With three detectors N_{thr} is reduced to the desired target of one photon. Without any further assumptions. This scaling follows a $1/n$ dependence as shown in Figure 9.

With increasing number of detectors in coincidence the detection efficiency of signal photons scales with the binomial sum as shown in eq. 16 in Sec. 4. To achieve a high overall detection efficiency, one may require a coincidence in k out of n detectors to see a signal. Using four out of seven detectors in coincidence retains the signal threshold of one photon and reaches a detection efficiency of > 0.95 assuming the efficiency of a single SPD to be $\epsilon_{\text{det}} = 0.8$. Using a four out of 10 coincidence reached a detection efficiency greater than 0.99. Table 5 summarizes coincidence configurations usable for different assumptions on the dark count rate. This shows that nine detectors with SPDs reach a signal threshold of one photon with dark count rates up to 50 Hz.

$f_{\text{DC}} (p_{\text{bkg}})$	$p_{\text{sig}}^{(k)} > 0.90$	$p_{\text{sig}}^{(k)} > 0.95$	$p_{\text{sig}}^{(k)} > 0.99$
5 Hz (0.015)	7/9	7/10	7/11
10 Hz (0.03)	8/10	8/11	9/13
20 Hz (0.06)	11/14	11/14	12/17

Table 5. Minimal coincidence configuration (k out of n cavities) required to reach a false positive rate below 10^{-10} , corresponding to approximately one background event per year. The rows correspond to different assumptions on the dark count rate $f_{\text{DC}} (p_{\text{bkg}}$ — probability of background photon in a single time window), while the columns indicate the required overall signal detection probability $p_{\text{sig}}^{(k)}$ of k coincident cavities. A single-cavity signal detection efficiency of $p_{\text{sig}} = 0.9$ is assumed. The coincidence time window used in the calculation is 3 ms.

We now turn to the estimate of the sensitivity to PBH mergers. We require that within the bandwidth of the cavity and within the assumed readout time of 1 ms (10 ms) the energy of at least one photon is deposited by the GW in the cavity. Using Eqs. 6 the required strain is calculated as a function of the PBH merger mass, see

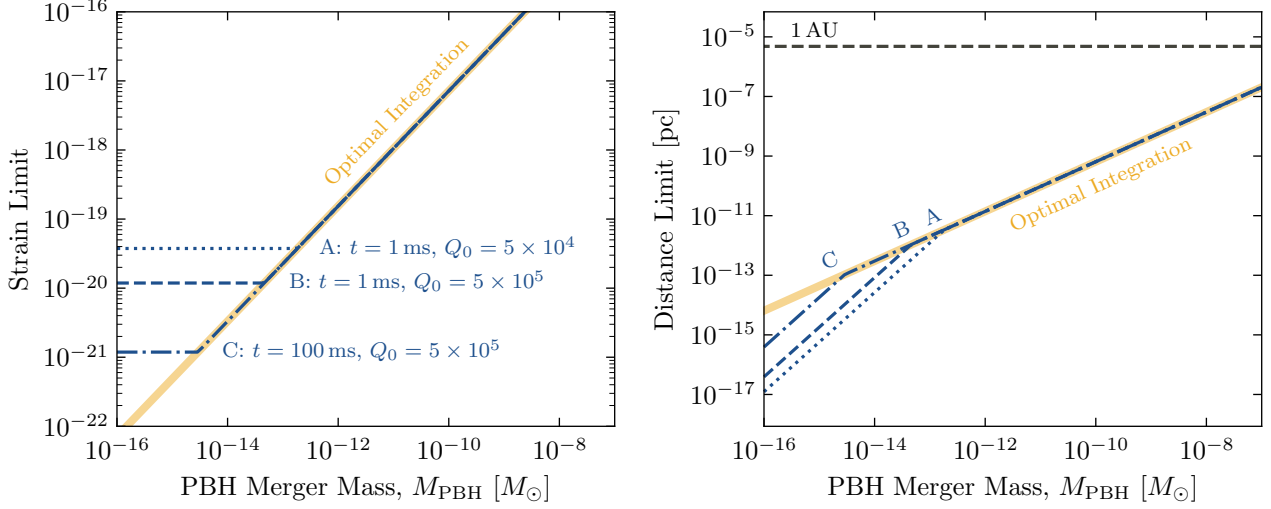


Fig. 10. The 95% confidence level limits on the sensitivity assuming a coincidence measurement with single photon detectors, where the number of coincidences is chosen to reach a signal threshold of one detected photon. For the appropriate coincidence configurations refer to Tab. 5. The coincidence window is taken to be long enough to allow the full transient signal to be included, as shown by the ‘Optimal Integration’ line, computed for $Q_0 = 5 \times 10^5$. Shorter coincidence (or readout) windows reduces the sensitivity; in this case, the quality factor becomes important as it changes the time the signal spends within the time window. We take three benchmark configurations to illustrate this (A, B, and C), as indicated by the broken lines. **Left:** The detectable strains with PBH merger mass. Lower PBH masses yield longer signals within the bandwidth of the cavity, such that the sensitivity saturates when the signal duration is longer than the coincidence time. **Right:** The distance reach after converting the strain limit to a distance for a given PBH merger mass. The broken lines are drawn for the same benchmark points as on the left panel. Also marked is $1 \text{ AU} \simeq 4.8 \times 10^{-6} \text{ pc}$.

Figure 10 (left). In this configuration, the strain limit decreases with increasing mass of the signal source. For signal durations exceeding the SPD measurement interval, the strain limit becomes independent of the source mass. The measurement duration of the SPD and the bandwidth of the cavity determine at which PBH mass and minimum strain the strain limit becomes constant. Increasing the signal threshold allows one to reach lower PBH masses at lower minimum strains, but decreases the sensitivity to fast signals at larger mass values.

The strain limit is converted to the distance reach, within which a PBH merger would be detected, as shown in Figure 10 (right).

The limiting factor is the requirement to deposit the energy of at least one photon in the detector. This yields sensitivity independent of the quality factor of the cavity and independent of the readout time of the SPD as long as the time the transient signal spent within the bandwidth of the cavity is smaller than the readout time. If the transients are slow, increased readout time windows increase the sensitivity. Alternatively, adjacent readout windows can be combined in software. Comparing these results to the expectations on the sensitivity of the power readout (Figure 7) shows a superior sensitivity for low PBH masses $< 10^{-13} M_\odot$ and sensitivity for large masses $M_{\text{PBH}} > 10^{-10} M_\odot$, which are not accessible with the power readout.

7 Conclusion and Outlook

The GRAVNET collaboration aims to establish a novel experimental platform dedicated to the research and development for the detection of high-frequency gravitational waves (HFGWs). The proposed strategy relies on the synchronous operation of multiple, geographically separated electromagnetic cavities immersed in strong magnetic fields, enabling the exploration of detection techniques based on the inverse Gertsenshtein effect in resonant systems. Beyond the search for potential signals, a central objective of GRAVNET is the systematic development, validation, and optimization of technologies capable of probing the largely unexplored HFGW domain.

The network configuration plays a crucial role in addressing one of the central experimental challenges: the discrimination of genuine gravitational signals from experimental noise. By exploiting time-coincidence and cross-correlation among distant detectors, the GRAVNET network enables robust background rejection, improves the achievable signal-to-noise ratio, and provides a framework for validating the gravitational origin of transient events. In addition, the spatial separation of the detectors allows the reconstruction of arrival times across the network, opening the possibility of constraining the direction of potential sources.

An important feature of the project is the development of resonant cavities capable of tuning over a broad range of frequencies. This capability is particularly relevant for the study of rapidly evolving HFGW signals. While we have explored the promise of such detectors to detect primordial black hole mergers, the theoretical framework developed here indicates that we will have sensitivities to a variety of well-motivated sources.

The GRAVNET network is designed to be an open and evolving experimental framework. Additional detector nodes may join the network as the project progresses, further increasing its sensitivity and robustness. Since gravitational waves interact universally with matter, the network can in principle incorporate a variety of detector technologies beyond resonant cavities. This flexibility allows GRAVNET to serve as a testbed for exploring different experimental strategies and identifying the most promising approaches to achieve competitive sensitivity in the high-frequency regime.

The GRAVNET project will proceed through a phased implementation:

- Phase I (Demonstration): Building upon the initial single non-superconducting cavity experiment, this phase will focus on commissioning the first three detectors located in Bonn, Mainz, and Frascati. The primary goal is to validate the time-synchronization and correlation-based data-analysis techniques required for efficient noise rejection and directional sensitivity.
- Phase II (Network Expansion): Expanding the GRAVNET infrastructure to four or more detectors distributed globally. A larger network will enhance coincidence-based background suppression, improve source localization capabilities, and establish a continuous monitoring program for transient HFGW events.
- Phase III (Sensitivity Goal): Optimizing the network through the deployment of advanced (possibly superconducting) cavities with increased volume (V) and magnetic field strength (B_0), with the aim of reaching sensitivities capable of probing the primordial black hole dark-matter paradigm in the asteroid mass window and constraining models of primordial gravitational-wave backgrounds.

Looking ahead, advances in quantum sensing may provide significant opportunities to further enhance detector performance. In particular, quantum measurement schemes based on entanglement [99] and distributed quantum sensing [100, 101] could improve the effective sensitivity of spatially separated detectors by enabling correlated measurements across the network. Initiatives such as the Fermilab quantum network IEQNET (Illinois Express Quantum Network) demonstrate the feasibility of long-distance entangled measurements and may offer a technological pathway toward implementing quantum-enhanced gravitational-wave detection strategies in the future.

By systematically exploring the largely uncharted HFGW spectrum and fostering the development of new experimental techniques, GRAVNET represents an important step toward opening a new observational window into the Universe. Whether through direct detection of high-frequency gravitational waves or through the technological advances developed along the way, the program has the potential to significantly deepen our understanding of gravity, the nature of dark matter, and the physics of the early Universe.

Acknowledgments

This research is primarily supported by the ERC-2024-SYG 101167211 grant (GRAVNET DOI: 10.3030/101167211), as well as by the Cluster of Excellence “Precision Physics, Fundamental Interactions, and Structure of Matter” (PRISMA++ EXC 2118/2) funded by the German Research Foundation (DFG) within the German Excellence Strategy (Project ID 390831469), and by the COST Action within the project COSMIC WISPerS (Grant No. CA21106). Views and opinions expressed are however those of the author(s) only and do not necessarily reflect

those of the European Union or the European Research Council Executive Agency. Neither the European Union nor the granting authority can be held responsible for them.

This publication is part of the grant PID2023-146686NB-C31 funded by MICIU/AEI/10.13039/501100011033/ and by FEDER, UE. IFAE is partially funded by the CERCA program of the Generalitat de Catalunya. D.B. acknowledges the support from the European Research Area (ERA) via the UNDARK project of the Widening participation and spreading excellence programme (project number 101159929). L.V. acknowledges support by Istituto Nazionale di Fisica Nucleare (INFN) through the Commissione Scientifica Nazionale 4 (CSN4) Iniziativa Specifica “Quantum Universe” (QGSKY). J.G. is funded by Grant No. CNS2023-143767, funded by MICIU/AEI/10.13039/501100011033 and by European Union NextGenerationEU/PRTR.

References

1. B. P. Abbott *et al.* (LIGO Scientific, Virgo), *Phys. Rev. Lett.* **116**, 061102 (2016), arXiv:1602.03837 [gr-qc] .
2. G. Agazie *et al.* (NANOGrav), *Astrophys. J. Lett.* **951**, L8 (2023), arXiv:2306.16213 [astro-ph.HE] .
3. P. Amaro-Seoane *et al.*, arXiv e-prints , arXiv:1702.00786 (2017), arXiv:1702.00786 [astro-ph.IM] .
4. N. Aggarwal *et al.*, *Living Rev. Rel.* **28**, 10 (2025), arXiv:2501.11723 [gr-qc] .
5. T. J. Clarke, E. J. Copeland, and A. Moss, *JCAP* **10**, 002 (2020), arXiv:2004.11396 [astro-ph.CO] .
6. M. Maggiore *et al.*, *JCAP* **03**, 050 (2020), arXiv:1912.02622 [astro-ph.CO] .
7. G. Janssen *et al.*, *PoS AASKA14*, 037 (2015), arXiv:1501.00127 [astro-ph.IM] .
8. A. I. Renzini, B. Goncharov, A. C. Jenkins, and P. M. Meyers, *Galaxies* **10**, 34 (2022), arXiv:2202.00178 [gr-qc] .
9. N. Aggarwal *et al.*, *Living Rev. Rel.* **24**, 4 (2021), arXiv:2011.12414 [gr-qc] .
10. M. Maggiore, *Gravitational Waves. Vol. 1: Theory and Experiments* (Oxford University Press, 2007).
11. D. Blas, J. Casalderrey-Solana, D. Mateos, and M. Sanchez-Garitaonandia, *Phys. Rev. Lett.* **136**, 101401 (2026), arXiv:2210.03171 [hep-th] .
12. B. Carr and F. Kuhnel, *SciPost Phys. Lect. Notes* **48**, 1 (2022), arXiv:2110.02821 [astro-ph.CO] .
13. A. M. Green and B. J. Kavanagh, *J. Phys. G* **48**, 043001 (2021), arXiv:2007.10722 [astro-ph.CO] .
14. B. Carr, K. Kohri, Y. Sendouda, and J. Yokoyama, *Rept. Prog. Phys.* **84**, 116902 (2021), arXiv:2002.12778 [astro-ph.CO] .
15. R. Abbott *et al.* (LVK), *Mon. Not. Roy. Astron. Soc.* **524**, 5984 (2023), [Erratum: *Mon. Not. Roy. Astron. Soc.* **526**, 6234 (2023)], arXiv:2212.01477 [astro-ph.HE] .
16. S. Shandera, D. Jeong, and H. S. G. Gebhardt, *Phys. Rev. Lett.* **120**, 241102 (2018), arXiv:1802.08206 [astro-ph.CO] .
17. G. F. Giudice, M. McCullough, and A. Urbano, *JCAP* **10**, 001 (2016), arXiv:1605.01209 [hep-ph] .
18. A. Berlin, D. Blas, R. Tito D’Agnolo, S. A. R. Ellis, R. Harnik, Y. Kahn, and J. Schütte-Engel, *Phys. Rev. D* **105**, 116011 (2022), arXiv:2112.11465 [hep-ph] .
19. G. Franciolini, A. Maharana, and F. Muia, *Phys. Rev. D* **106**, 103520 (2022), arXiv:2205.02153 [astro-ph.CO] .
20. S. Schenk, K. Schmieden, and P. Schwaller, (2025), arXiv:2512.20592 [hep-ph] .
21. D. Blas, Y. Chen, Y. Liu, Y. Shang, and J. Shu, (2026), arXiv:2601.03341 [hep-ph] .
22. E. G. M. Ferreira, *Astron. Astrophys. Rev.* **29**, 7 (2021), arXiv:2005.03254 [astro-ph.CO] .
23. A. Arvanitaki, S. Dimopoulos, S. Dubovsky, N. Kaloper, and J. March-Russell, *Phys. Rev. D* **81**, 123530 (2010), arXiv:0905.4720 [hep-th] .
24. R. Brito, V. Cardoso, and P. Pani, *Lect. Notes Phys.* **906**, pp.1 (2015), arXiv:1501.06570 [gr-qc] .
25. A. Arvanitaki and S. Dubovsky, *Phys. Rev. D* **83**, 044026 (2011), arXiv:1004.3558 [hep-th] .
26. M. Baryakhtar, M. Galanis, R. Lasenby, and O. Simon, *Phys. Rev. D* **103**, 095019 (2021), arXiv:2011.11646 [hep-ph] .
27. S. J. Witte and A. Mummery, *Phys. Rev. D* **111**, 083044 (2025), arXiv:2412.03655 [hep-ph] .
28. A. Berlin, D. Blas, R. Tito D’Agnolo, S. A. R. Ellis, R. Harnik, Y. Kahn, J. Schütte-Engel, and M. Wentzel, *Phys. Rev. D* **108**, 084058 (2023), arXiv:2303.01518 [hep-ph] .
29. A. Ringwald and C. Tamarit, *Phys. Rev. D* **106**, 063027 (2022), arXiv:2203.00621 [hep-ph] .
30. J. Ghiglieri, G. Jackson, M. Laine, and Y. Zhu, *JHEP* **07**, 092 (2020), arXiv:2004.11392 [hep-ph] .
31. S. Vagnozzi and A. Loeb, *Astrophys. J. Lett.* **939**, L22 (2022), arXiv:2208.14088 [astro-ph.CO] .
32. R. Schnabel and M. Korobko, *Sci. Rep.* **15**, 25733 (2025), arXiv:2409.03019 [astro-ph.IM] .
33. C. M. Jungkind, B. C. Seymour, A. Laeuger, and Y. Chen, *Phys. Rev. D* **113**, 024057 (2026), arXiv:2506.08315 [gr-qc] .
34. J. Heisig, (2025), arXiv:2510.13957 [gr-qc] .

35. M. Goryachev and M. E. Tobar, Phys. Rev. D **90**, 102005 (2014), [Erratum: Phys.Rev.D 108, 129901 (2023)], arXiv:1410.2334 [gr-qc] .
36. Y. Kim *et al.*, (2025), arXiv:2511.17817 [hep-ex] .
37. R. Ballantini *et al.*, (2005), arXiv:gr-qc/0502054 .
38. M. E. Gertsenshtein and V. I. Pustovoit, Sov. Phys. JETP **16**, 433 (1962).
39. A. Berlin *et al.*, (2022), arXiv:2203.12714 [hep-ph] .
40. C. Gatti, L. Visinelli, and M. Zantedeschi, Phys. Rev. D **110**, 023018 (2024), arXiv:2403.18610 [gr-qc] .
41. J. Gué, T. Krokotsch, and G. Moortgat-Pick, (2026), arXiv:2602.08507 [gr-qc] .
42. W. Ratzinger, S. Schenk, and P. Schwaller, JHEP **08**, 195 (2024), arXiv:2404.08572 [gr-qc] .
43. Y. Borysenkova, T. Kvietkauskas, D. Amaral, S. Kalia, and D. Blas, (2026), arXiv:2603.xxxxx [hep-ph] .
44. M. Bertani, A. Cecchetti, B. Dulach, F. Fabbri, M. Giardoni, A. Lanaro, V. Lucherini, T. Bressani, A. Feliciello, A. Filippi, *et al.*, Nuclear Physics B-Proceedings Supplements **78**, 553 (1999).
45. M. Modena, (1997).
46. D. Alesini *et al.*, Phys. Dark Univ. **42**, 101370 (2023), arXiv:2309.00351 [physics.ins-det] .
47. A. Wagner *et al.* (ADMX), Phys. Rev. Lett. **105**, 171801 (2010), arXiv:1007.3766 [hep-ex] .
48. C. Ligì, G. Delle Monache, R. Ricci, and C. Sanelli, EPAC 2002 Proceedings , 2523 (2002).
49. S. Chaudhuri, K. D. Irwin, P. W. Graham, and J. Mardon, (2019), arXiv:1904.05806 [hep-ex] .
50. T. Schneemann, K. Schmieden, and M. Schott, (2023), arXiv:2308.08337 [hep-ex] .
51. A. Alimenti, K. Torokhtii, D. Di Gioacchino, C. Gatti, E. Silva, and N. Pompeo, Instruments **6**, 1 (2021), arXiv:2112.12775 [physics.ins-det] .
52. D. Alesini *et al.*, Phys. Rev. D **99**, 101101 (2019), arXiv:1903.06547 [physics.ins-det] .
53. “Capp: Superconducting cavity for dark matter axion search,” https://agenda.infn.it/event/20431/contributions/137693/attachments/82473/108372/2021_June_PATRAS_Meeting_Danho_Ahn_v5.pdf (2021).
54. D. Ahn *et al.*, Phys. Rev. Appl. **17**, L061005 (2022).
55. K. Schmieden, T. Schneemann, M. Schott, M. Unni, H. Bekker, A. Wickenbrock, and D. Budker, (2024), arXiv:2412.14958 [cond-mat.supr-con] .
56. D. Alesini *et al.*, Phys. Rev. D **106**, 052007 (2022), arXiv:2208.12670 [hep-ex] .
57. M. Lawson, A. J. Millar, M. Pancaldi, E. Vitagliano, and F. Wilczek, Phys. Rev. Lett. **123**, 141802 (2019), arXiv:1904.11872 [hep-ph] .
58. R. Capdevilla, G. B. Gelmini, J. Hyman, A. J. Millar, and E. Vitagliano, Phys. Rev. D **112**, 055011 (2025), arXiv:2412.14450 [hep-ph] .
59. J. Lindahl, R. Balafendiev, G. Kaur, G. Singh, A. Gallo Rosso, J. Conrad, J. E. Gudmundsson, and J. Jeong, Phys. Rev. Applied **25**, 024073 (2026), arXiv:2508.18145 [hep-ex] .
60. N. Kowitz, R. Balafendiev, D. Sun, M. Wooten, A. Droster, M. A. Gorlach, K. van Bibber, and P. A. Belov, Phys. Rev. Applied **20**, 044051 (2023), arXiv:2306.15734 [hep-ex] .
61. C. M. Caves, Phys. Rev. D **26**, 1817 (1982).
62. S. K. Lamoreaux, K. A. van Bibber, K. W. Lehnert, and G. Carosi, Phys. Rev. D **88**, 035020 (2013).
63. C. Gatti, in *14th Workshop on Low Temperature Electronics* (2021).
64. M. Mück and R. McDermott, Superconductor Science and Technology **23**, 093001 (2010).
65. L. Zhong, E. P. Menzel, R. D. Candia, P. Eder, M. Ihmig, A. Baust, M. Haeberlein, E. Hoffmann, K. Inomata, T. Yamamoto, Y. Nakamura, E. Solano, F. Deppe, A. Marx, and R. Gross, New Journal of Physics **15**, 125013 (2013).
66. N. Roch, E. Flurin, F. Nguyen, P. Morfin, P. Campagne-Ibarcq, M. H. Devoret, and B. Huard, Phys. Rev. Lett. **108**, 147701 (2012).
67. L. S. Kuzmin, A. S. Sobolev, C. Gatti, D. Di Gioacchino, N. Crescini, A. Gordeeva, and E. Il'ichev, IEEE Trans. Appl. Supercond. **28**, 2400505 (2018).
68. M. Mück, M. O. Andre, J. Clarke, J. Gail, and C. Heiden (ADMX), Nucl. Phys. B Proc. Suppl. **72**, 145 (1999).
69. D. Aybas *et al.*, Phys. Rev. Lett. **126**, 141802 (2021), arXiv:2101.01241 [hep-ex] .
70. A. J. Brady, C. Gao, R. Harnik, Z. Liu, Z. Zhang, and Q. Zhuang, PRX Quantum **3**, 030333 (2022).
71. W. Górecki, A. Riccardi, and L. Maccone, Phys. Rev. Lett. **129**, 240503 (2022).
72. H. Shi and Q. Zhuang, npj QUantum Inf **9** (2023).
73. J. Koch, T. M. Yu, J. Gambetta, A. A. Houck, D. I. Schuster, J. Majer, A. Blais, M. H. Devoret, S. M. Girvin, and R. J. Schoelkopf, Phys. Rev. A **76**, 042319 (2007).
74. J. S. D. Schuster, A. Houck *et al.*, Nature **445**, 515 (2007).
75. A. D'Elia *et al.*, Applied Sciences **14** (2024), 10.3390/app14041478.
76. R. Moretti *et al.*, IEEE Transactions on Quantum Engineering **7**, 1 (2026).
77. A. S. P. Komnang *et al.*, IL NUOVO CIMENTO **49 C**, 77 (2026).

78. A. DElia *et al.*, (2025), arXiv:2509.17160 [quant-ph] .
79. C. Gatti *et al.*, IEEE Transactions on Applied Superconductivity **33**, 1 (2023).
80. A. D'Elia *et al.*, IEEE Trans. Appl. Supercond. **33**, 1500109 (2023), arXiv:2302.07556 [quant-ph] .
81. K. K. K. Inomata, Z. Lin *et al.*, Nat Commun **7**, 12303 (2016).
82. R. Lescanne, S. Deléglise, E. Albertinale, U. Réglade, T. Capelle, E. Ivanov, T. Jacqmin, Z. Leghtas, and E. Flurin, Phys. Rev. X **10**, 021038 (2020).
83. J.-C. Besse, S. Gasparinetti, M. C. Collodo, T. Walter, P. Kurpiers, M. Pechal, C. Eichler, and A. Wallraff, Phys. Rev. X **8**, 021003 (2018).
84. Z. T. S. Kono, K. Koshino *et al.*, Nature Phys **14**, 546 (2018).
85. S. Chen, H. Fukuda, T. Inada, T. Moroi, T. Nitta, and T. Sichanugrist, Phys. Rev. D **110**, 115021 (2024).
86. A. V. Dixit, S. Chakram, K. He, A. Agrawal, R. K. Naik, D. I. Schuster, and A. Chou, Phys. Rev. Lett. **126**, 141302 (2021).
87. C. L. Degen, F. Reinhard, and P. Cappellaro, Rev. Mod. Phys. **89**, 035002 (2017).
88. K. Backes, D. Palken, S. Kenany, *et al.*, Nature **590**, 238–242 (2021).
89. B. P. Abbott *et al.* (KAGRA, LIGO Scientific, Virgo, VIRGO), Living Rev. Rel. **21**, 3 (2018), arXiv:1304.0670 [gr-qc] .
90. S. Afach, B. C. Buchler, D. Budker, C. Dailey, A. Derevianko, V. Dumont, N. L. Figueroa, I. Gerhardt, Z. D. Grujić, H. Guo, C. Hao, P. S. Hamilton, M. Hedges, D. F. Jackson Kimball, D. Kim, S. Khamis, T. Kornack, V. Lebedev, Z.-T. Lu, H. Masia-Roig, M. Monroy, M. Padniuk, C. A. Palm, S. Y. Park, K. V. Paul, A. Penafior, X. Peng, M. Pospelov, R. Preston, S. Pustelny, T. Scholtes, P. C. Segura, Y. K. Semertzidis, D. Sheng, Y. C. Shin, J. A. Smiga, J. E. Stalnaker, I. Sulai, D. Tandon, T. Wang, A. Weis, A. Wickenbrock, T. Wilson, T. Wu, D. Wurm, W. Xiao, Y. Yang, D. Yu, and J. Zhang, Nature Physics **17**, 1396 (2021).
91. S. Afach, D. Aybas Tumturk, H. Bekker, B. C. Buchler, D. Budker, K. Cervantes, A. Derevianko, J. Eby, N. L. Figueroa, R. Folman, D. Gavilán-Martín, M. Givon, Z. D. Grujić, H. Guo, P. Hamilton, M. P. Hedges, D. F. Jackson Kimball, S. Khamis, D. Kim, E. Klinger, A. Kryemadhi, X. Liu, G. Łukasiewicz, H. Masia-Roig, M. Padniuk, C. A. Palm, S. Y. Park, H. R. Pearson, X. Peng, M. Pospelov, S. Pustelny, Y. Rosenzweig, O. M. Ruimi, T. Scholtes, P. C. Segura, Y. K. Semertzidis, Y. C. Shin, J. A. Smiga, Y. V. Stadnik, J. E. Stalnaker, I. A. Sulai, D. Tandon, K. Vu, A. Weis, A. Wickenbrock, T. Z. Wilson, T. Wu, W. Xiao, Y. Yang, D. Yu, F. Yu, J. Zhang, and Y. Zhao, Annalen der Physik **536**, 2300083 (2024), <https://onlinelibrary.wiley.com/doi/pdf/10.1002/andp.202300083> .
92. B. M. Roberts, G. Blewitt, C. Dailey, M. Murphy, M. Pospelov, A. Rollings, J. Sherman, W. Williams, and A. Derevianko, Nature Commun. **8**, 1195 (2017), arXiv:1704.06844 [hep-ph] .
93. O. Tretiak, X. Zhang, N. L. Figueroa, D. Antypas, A. Brogna, A. Banerjee, G. Perez, and D. Budker, Phys. Rev. Lett. **129**, 031301 (2022).
94. A. V. Gramolin, D. Aybas, D. Johnson, J. Adam, and A. O. Sushkov, Nature Physics **17**, 79 (2021).
95. B. S. Sathyaprakash and B. F. Schutz, Living Reviews in Relativity **12** (2009), 10.12942/lrr-2009-2.
96. G. Turin, IRE Transactions on Information Theory **6**, 311 (1960).
97. R. H. Dicke, Rev. Sci. Instrum. **17**, 268 (1946).
98. L. Pallegoix, J. Travesedo, A. S. May, L. Balembois, D. Vion, P. Bertet, and E. Flurin, (2025), arXiv:2501.07354 [quant-ph] .
99. A. J. Brady, C. Gao, R. Harnik, Z. Liu, Z. Zhang, and Q. Zhuang, PRX Quantum **3**, 030333 (2022), arXiv:2203.05375 [quant-ph] .
100. Y.-f. Cai, L. Visinelli, and S.-F. Yan, (2025), arXiv:2510.15031 [hep-ph] .
101. Y. Wang *et al.*, Nature **650**, 314 (2026).